Sensitivity Analysis of the High-Frequency-Link MMC to DC Link Voltage Ripples in a Back-to-Back Connected MMC-Based Power Electronic Transformer

Vishnu Narayan Vipin, *Member, IEEE*, and Ned Mohan, *Fellow, IEEE*

***Abstract*—Integrating renewables and storage to the medium voltage grid (5–34.5 kV), allows for high power export while minimizing conduction losses. Recent converter topologies involve cascading low-voltage (LV) submodules (SMs) to meet grid voltage levels, enabling power extraction from LV storage units and PV arrays. This article focuses on studying such a topology with a common controllable high voltage (HV) dc link for the grid side MMC (GS-MMC) and the high-frequency link MMC (HF-MMC). The storage units and renewable sources like wind and solar provide power through the LV side of a high-frequency (HF) step-up transformer, which is processed by the HF-MMC and GS-MMC, before reaching the grid. In this configuration, GS-MMC injects voltage ripples into the common HV dc link due to the employed pulse width modulation (PWM) scheme for switching its SMs. This injected ripple interacts with the switching modulation scheme of the HF-MMC SMs, resulting in voltage oscillations in the HF-MMC capacitors and current flow through its phase legs. The article provides a mathematical basis that explains the sensitivity of the HF-MMC response to different frequencies of voltage ripple. It also offers theoretical support for the observed resonant peaks in the frequency response of the HF-MMC phase legs, the mechanism behind the unique resonance and closed-form expressions for these resonant frequencies. An approximate equivalent circuit model for the HF-MMC phase legs is provided towards this end. The analysis is validated through MATLAB/Simulink simulations and OPAL-RT based Hardware-In-Loop real-time simulations, as well as experimental results obtained using a scaled-down laboratory prototype.**

***Index Terms*—Back-to-Back MMCs, dc link voltage ripples, dc side equivalent circuit and modeling, high-frequency link MMC, power electronic transformer (PET).**

Nomenclature

f_s	HF-MMC switching frequency/output voltage fundamental frequency.
f	External ripple frequency at the dc link.
T_{FRF}/T_{VRF}	Time period of one cycle of the follower/variant resonant frequency.
N	No. of submodules per arm of the MMC.
T	Time period of injected sinusoidal voltage in the dc link.
L, R	Total arm inductance/resistance in a HF-MMC phase leg.
C	Effective HF-MMC submodule capacitance in an arm.
V_{mod}	The sum of the HF-MMC submodule output voltages in a phase leg.
N_{gcd}	The ratio of the switching frequency to $GCD(f, f_s)$.
N_f	The ratio of the external ripple frequency to $GCD(f, f_s)$.
θ	Complex eigenvalue angle in the initial condition vector matrix formulation.
v	Ratio of half switching cycle period and $L-C$ resonant frequency in rad/sec.
h	Fraction of phase angle spanned by ripple frequency in half a switching cycle.

Received 19 May 2024; revised 16 September 2024 and 17 December 2024; accepted 28 January 2025. Date of publication 4 February 2025; date of current version 20 March 2025. Recommended for publication by Associate Editor Y. Li. *(Corresponding author: Vishnu Narayan Vipin.)*

Vishnu Narayan Vipin is with Rivian Automotive LLC, Power Electronics Control Group, Torrance, CA 90503 USA (e-mail: vnarayan57@gmail.com).

Ned Mohan is with Electrical and Computer Engineering Department, University of Minnesota, Minneapolis, MN 55455 USA.

Color versions of one or more figures in this article are available at https://doi.org/10.1109/TPEL.2025.3538605.

Digital Object Identifier 10.1109/TPEL.2025.3538605

I. Introduction

THE integration of renewables and storage to the medium voltage grid (5–34.5 kV) is crucial for sustainable power generation, allowing extraction of megawatts of power [1], [2], [3], [4], [5], [6]. Wind turbines, with their large-scale power output, are well suited for interfacing with the medium voltage grid [7], [8], [9]. The growing penetration of wind turbines is driving sustainability goals and highlighting the need to improve cost and efficiency in wind power generation [10], [11], [12].

In comparison to current wind turbine integration schemes as shown in Fig. 1(a) (top) which use a 60-Hz transformer [7], [8], [9], the topology studied in this article shown in Fig. 1(b) [13], [14], [15], [16], [17], [18] is based on the back-to-back connected MMCs-based Power Electronic Transformer (PET). This avoids high currents in the long cables from the nacelle to ground where the power electronic converter and heavy 60-Hz transformer are located and also significantly decreases the transformer's weight [19], [20] allowing to integrate it into the nacelle alongside the converter.

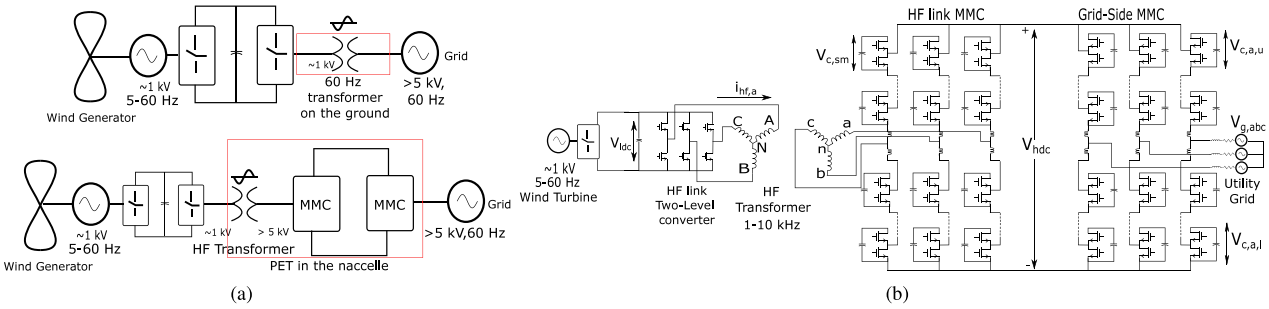

Fig. 1. (a) Existing grid-interface scheme for wind turbine generators (top) versus studied BB-MMC PET-based interface scheme (bottom), and (b) detailed circuit diagram of the studied BB-MMC PET architecture.

In VSC-HVDC systems, MMCs use a large number of submodules connected in cascade to achieve high transmission voltage levels [21], [22], [23]. In contrast, the studied BB-MMC architecture uses a few submodules to reach medium-voltage grid level. The distributed capacitance of transmission lines causes the dc link in VSC-HVDC systems to behave as a stable dc voltage source, while the studied topology presents a lower effective dc bus capacitance due to the submodule capacitors. This makes the dc bus sensitive to switching modulation schemes employed in back-to-back connected MMCs.

In order to meet the grid voltage level, submodules (SMs) with lower voltage ratings are cascaded. In comparison to other medium voltage cascaded power converter topologies [1], [2], this topology based on back-to-back connected MMCs-based PETs [13], [14], [15], [16], [17], [18] is better suited to extract power from high-power three-phase sources such as mega-watt rated wind turbines and have customizable number of HF transformers [24]. The single controllable HV dc link for virtual inertia support [16], and control of power through the customizable number of HF links improves the reliability and renders the control simple.

Back-to-back connected MMC configurations have been documented in various studies [25], [26], [27], [28], [29] for integrating medium voltage grids, railway traction, and certain motor drive applications. In some cases, these MMC setups are used to generate ac voltages at line frequencies or lower ones like $10-50$ Hz[25], [27]. Another configuration involves the HF-MMC sharing the dc link with GS-MMC and being connected to the HF transformer to produce high-frequency ac output voltages (>1 kHz $-$ 50 kHz) [18], [24]. In either of the cases, the PWM output of the cascaded half-bridge modules forms the dc bus voltages but introduces switching ripple on top of the dc value [17]. This article investigates how these dc voltage ripples uniquely impact the behavior of HF-MMC due to the close proximity of its output voltage frequency to the PWM frequency of GS-MMC as in [18] and [24], leading to a resonant effect that is studied here along with a mathematical foundation for this phenomenon.

AC admittance modeling of the MMC was extensively studied in [21], [22], [30], [31], and [32]. In these references, the effect of different closed loop control schemes on the ac admittance of the converter was studied [30], [31], [32] and the impedance stability of the converter in a wind farm setting was studied [21], [22]. In this analysis, the frequency response of the HF-MMC phase legs in response to switching ripple at the dc link is studied by approximating the HF-MMC arm voltages as simple square waves and it is shown that the approximation holds good at high modulation index operation of the HF-MMC such as with trapezoidal modulation in [33] and [34] and for unity DPF operation at the HF-link as in [18].

The authors in [16] and [17] provided a fundamental control scheme for operating the back-to-back connected MMC-based PET, without delving into the specifics of HF-side closed-loop control and harmonic mitigation. In another study, the control of the HF-MMC and the two-level voltage source converter is developed to optimize power transfer across the HF link [18]. In [24], a novel topology for integration of heterogeneous energy sources by sharing a common dc link with multiple MMCs was discussed. However, none of these instances address the sensitivity of the HF-MMC to voltage ripples injected into the shared dc link by other MMCs. This work aims to investigate and provide answers to several key questions.

Q1 : What causes resonance behavior at multiple frequencies of dc link voltage ripple in HF-MMCs?

Q2 Can we derive closed-form expressions for these frequencies as functions of topology circuit parameters? Can we design modulation schemes and select switching frequencies for MMCs sharing a common dc link based on such expressions?

Q3 What are the unique characteristics of this resonance behavior? How can we utilize it in other applications? How does it differ from regular L-C circuit resonance?

In this regard, this work presents three key advancements as follows.

1) A theoretical foundation was developed to explain the resonance behavior arising due to the modulation of the HF-MMC SMs which shapes the impedance behavior of the SM capacitors along with the arm inductors (L_{arm}) in such a way that there are resonant peaks at certain frequencies of ripple. To explain this

a) In Section II, the basic circuit operation of the BB-MMCs is provided and the origin of the dc link voltage ripples are explained.

b) Then, an equivalent circuit for the operation of the HF-MMC phase legs is introduced in Section III-A.

c) Using the equivalent circuit, it is explained in Section III-B that the SM capacitances of the upper and lower arms in

the HF-MMC get inserted in their phase legs in alternating half-cycle intervals of the switching frequency to form R-L-C circuits. Further, a Fourier analysis expression for the sum of the HF-MMC submodule voltages is derived in Section III-B.

d) Using the Fourier analysis expression, it is shown that initial conditions of the arm inductor currents and submodule capacitor voltages at the beginning of these half-cycles take unique sets of values dependent on the frequency of ripple in Section III-C. A mathematical framework is established in Section III-C, to explain how these initial conditions play a role in eliciting a resonance-like behavior observed in the HF-MMC at certain frequencies of ripple.

2) *Closed-Form Frequency Solutions:* The article derives closed-form expressions as shown in (34), (36), and (37) for the frequencies at which the HF-MMC exhibits resonance. This analytical approach facilitates the design of modulation schemes and selection of switching frequencies for multiple MMCs sharing a common dc link with the HF-MMC.

3) *Applications:* The study reveals that one of the resonant frequencies of the HF-MMC exhibits independence from the circuit's L-C parameters. Notably, other resonant frequencies are demonstrably dependent on both this "invariant" resonance and the L-C characteristics. As described in Section IV, this discovery presents potential advantages in applications requiring stable resonant frequencies despite variations in inductance, such as wireless power transfer and radio frequency (RF) systems [35], [36].

4) *Results:* Finally in Section V, detailed results obtained from MATLAB/SIMULINK simulations, OPAL-RT Hardware-In-Loop real-time simulations, and the experimental hardware prototype are provided to verify the validity of the presented analysis.

II. Basic Circuit Operation and Origin of DC Link Ripples in the Back-to-Back Connected MMCs

The detailed circuit diagram of the studied power circuit is shown in Fig. 1(b). It is to be noted that the HF-MMC and the GS-MMC are directly connected as shown and that it is not an HVDC line. The entire BB-MMC, the HF-Transformer, and the BB-2L-VSC (wind turbine converter–back-to-Back connected two-level voltage source converter) are to be housed in the wind turbine nacelle.

The GS-MMC submodules are modulated using phase-shifted carrier sine-triangle PWM (PSC-PWM) ensuring minimum carrier frequency harmonics in the output voltage. PSC-PWM is especially suited when the number of submodules in the MMC is small as is the case here. The effective switching frequency harmonics in the output voltage are at $2N$ times the switching frequency of each submodule. The HF-MMC is modulated using nearest-level modulation and the output waveform is a sinusoidal stepped waveform. The switching frequencies of both the HF-MMC and HF side 2L-VSC are the same as the output voltage fundamental frequency across the transformer. The HF side 2L-VSC operates in a six-step mode since there

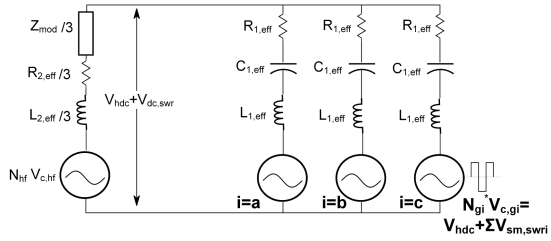

Fig. 2. Simplified diagram of the back-to-back MMC for HF-MMC sensitivity analysis.

are six steps in every fundamental cycle of its line-neutral voltage waveform. Both sides of the HF transformer do not see PWM waveforms to limit the dv/dt stresses involved if, e.g., a carrier frequency at ten times the HF link frequency is used for modulation.

The GS-MMC controls the currents drawn from the grid for V_{hdc} control, reactive power support to the grid, operation during grid unbalance and faults, virtual inertia support to the grid for frequency regulation and other grid ancillary services. The HF-MMC ensures minimum conduction losses in the HF-link by current harmonic control and controlling the currents to be at unity displacement power factor with the HF 2L-VSC. The HF 2L-VSC maintains the low voltage dc link at the commanded reference value and the WT 2L-VSC is involved in tracking the wind turbine's maximum power point.

In Fig. 2, the arm resistances and inductances have been grouped into an effective inductance and resistance in each phase leg. The switching ripple with frequency components around carrier harmonics and its multiples result in each leg due to the sum of the submodule PWM output voltages in the grid side MMC [17]. They are marked as $\Sigma V_{sm,swr}$ or $N_g^* V_{c,g}$ in Fig. 2. N_g^* is the instantaneous number of submodules turned ON in a phase-leg of the GS-MMC.

With the output fundamental frequency of 60 Hz at the GS-MMC, the ripple frequencies in the dc link are much greater in comparison. For this case, the terminal model of the submodule output voltages behave like a simple capacitance of value $C_{g,sm}/N$ as explained in Section III. The three legs of the HF-MMC are represented by the branch containing the impedance $Z_{mod}/3$. Here, Z_{mod} is the terminal impedance model of HF-MMC submodules. An expression H, for the transfer ratio of the SM switching ripples from the GS-MMC legs to the dc link is given as follows:

$$
\begin{aligned}
Z_{hf} &= Z_{mod} + R_{2,eff} + s\,L_{2,eff},\\
Z_g &= \frac{1}{s\,C_{1,eff}} + R_{1,eff} + s\,L_{1,eff}\\
Z_p &= \frac{Z_{hf}}{3} || \frac{Z_g}{2}\\
H &= \frac{Z_p}{Z_p + Z_g} = \frac{V_{dc,swr}}{\Sigma V_{sm,swr}}, C_{1,eff} = C_{g,sm}/N. \qquad (1)
\end{aligned}
$$

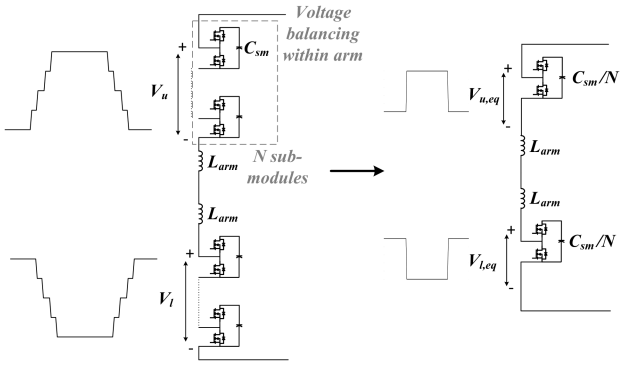

Fig. 3. Approximation of the HF-MMC operation with the equivalent circuit used in the analysis.

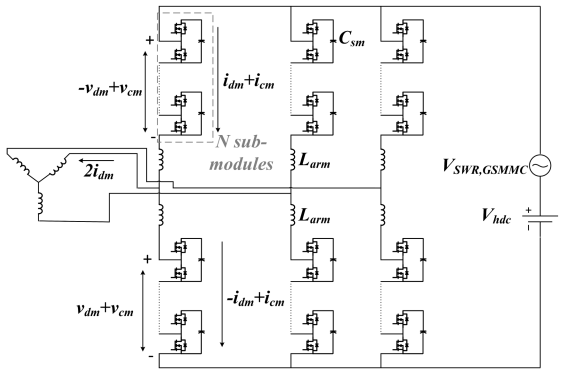

Fig. 4. AC port currents and decoupling of associated effect for current analysis.

III. DC Side Modeling of the HF-MMC Phase Legs

A. Premise and Assumptions

1) Equivalent Circuit of HF-MMC Phase Legs: This section analyzes the impact of dc-link switching ripple on a HF-MMC using an equivalent circuit of its phase legs as shown in Fig. 5. The half-bridge capacitors are assumed pre-charged to half the dc-link voltage (V_{hdc}). To isolate the ripple component, the dc bias voltage is removed, allowing the capacitor voltages to be modeled as variations around zero induced by the sinusoidal ripple in the dc link.

To further elaborate the approximation in deriving the equivalent circuit, Fig. 3 shows that each of the HF-MMC arms with N submodules have been replaced by a single half-bridge with submodule capacitance of value C_{sm}/N. The voltage balancing algorithm of the submodule capacitor voltages within an arm allows modeling the voltages of the submodule capacitors to be varying together in a single capacitance of value C_{sm}/N. However, this equivalent circuit is an approximation of the stepped arm voltage waveform by a square voltage waveform which happens when all the submodules of the HF-MMC arms simultaneously get inserted and bypassed without any intermediate steps in the arm voltages. This approximation holds well for the presented analysis if the HF-MMC operating modulation index is high [18], [33], [34] and at lower modulation indices the behavior of the HF-MMC deviates further away from this approximated equivalent circuit. In Section V-E, the magnitude sweep of the HF-MMC under different modulation indices are overlayed for comparison. As mentioned in III-A5, certain key frequency domain characteristics still hold at lower modulation indices and the analysis in this article provides insights into mechanism behind the resonance behavior at the various resonant frequencies.

2) High Modulation Index Approximation: For high modulation indices ($m_a > 0.875$ as shown in (2) for an example of $N = 4$), all submodules in one arm (upper or lower) are inserted during each half-cycle of the switching frequency (f_s). This simplifies the model by allowing lumping of the submodule capacitors in each arm into a single equivalent capacitance (C_{sm}/N) at the dc side of the half-bridges. Similarly, the arm inductances and resistances are combined into a single equivalent element ($2L_{arm}$ and $2R_{arm}$) for each arm

$$\begin{aligned} m_a &= 0.5 \pm 0.5\,(m_{hf})\,sin(\omega_s t), 0 \le m_{hf} \le 1 \\ N_{ON} &= round_{0.5}(N m_a) \\ m_a &\ge 0.875, \text{ all 4 modules ON} \\ 0.875 > m_a &\ge 0.625, \text{ 3 modules ON} \\ 0.625 > m_a &\ge 0.375, \text{ 2 modules ON} \\ 0.375 > m_a &\ge 0.125, \text{ 1 modules ON} \\ 0.125 > m_a &\ge 0, \text{ 0 modules ON.} \end{aligned} \tag{2}$$

3) Switching Pulses and Square Wave Approximation: The half-bridges receive switching signals (gate pulses) at the frequency of the HF-MMC's ac output voltage (f_s) as per (2). At high modulation indices, these pulses can be approximated as a single switching signal for the upper arm and a corresponding out-of-phase signal for the lower arm as shown in Fig. 5.

4) AC Port Decoupling: In Fig. 4, the differential and common mode voltage components in the upper and lower arms of the HF-MMC along with the associated differential mode output currents and the common mode circulating currents in a typical MMC operation are marked. The differential mode voltage created between the upper and lower arms of the HF-MMC due to the dc link ripples can be analytically shown to be zero by calculating the expression in (19). The differential mode currents flowing through the upper and lower arms of the HF-MMC which result in ac port currents are assumed to have negligible effect on the submodule capacitor voltages since the submodule capacitance values are designed so that the fundamental frequency odd harmonic differential mode currents and the even harmonic circulating currents result in a small percentage ripple (typically 2%–4% [37]). These submodule voltage ripples arising due to regular ac port currents and not due to the PWM switching ripple injected into the dc link have been neglected in this analysis. To further validate this simplification, the comparison of the time domain plots of V_{mod} along with HF-MMC arm currents have been added in Section V-G under the case of rated full load connected to the ac terminals and with ac terminals disconnected.

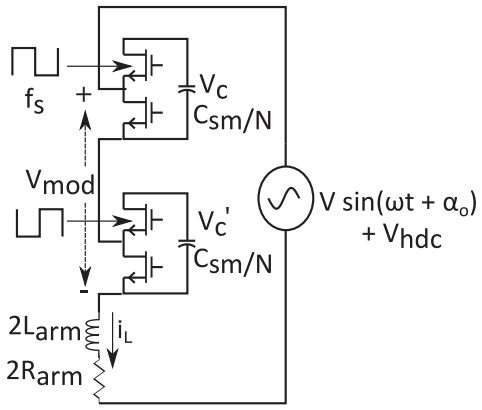

Fig. 5. Equivalent circuit to model the frequency response of the HF-MMC phase legs to voltage ripples in the DC link.

5) Model Accuracy and Applicability: While the equivalent circuit model (Fig. 5) is most accurate at high modulation indices, Section V demonstrates that key characteristics of the dc-link impedance frequency response remain valid at lower modulation indices as well.

B. Frequency Domain Analysis

To start with the analysis, it is observed that in each half-cycle of the switching frequency f_s, the circuit in Fig. 5 reduces to an R-L-C circuit. The time domain equation of the resulting RLC circuit with initial conditions on lumped arm inductor current and lumped submodule capacitor voltage is shown as follows:

$$V\sin(\omega(t-t_o)+\alpha) = 2\,L_{arm}\frac{di_L(t)}{dt} + i_L(t)\,2R_{arm} + \frac{N}{C_{sm}}\int_{to}^{t} i_L(t)\,dt. \tag{3}$$

The Laplace transform of the voltage equation of such an R-L-C circuit is shown as follows:

$$V\frac{\omega\cos(\alpha)+s\sin(\alpha)}{(s^2+\omega^2)} = L\,sI(s) - L\,I_{Lo} + I(s)\,R + \frac{1}{C}\frac{I(s)}{s} + \frac{V_{co}}{s} \tag{4}$$

$$V_c(x) = V_{co}\cos\left(\frac{x-\alpha}{\omega\sqrt{LC}}\right) + \sqrt{\frac{L}{C}}\,I_{Lo}\sin\left(\frac{x-\alpha}{\omega\sqrt{LC}}\right) - \frac{V}{\omega^2LC-1}\sin(x) + \frac{V}{\omega^2LC-1}\left(\cos\left(\frac{x-\alpha}{\omega\sqrt{LC}}\right)\times\sin(\alpha)+\omega\sqrt{LC}\cos(\alpha)\sin\left(\frac{x-\alpha}{\omega\sqrt{LC}}\right)\right) \tag{5}$$

$$i_L(x) = I_{Lo}\cos\left(\frac{x-\alpha}{\omega\sqrt{LC}}\right) - \sqrt{\frac{C}{L}}\,V_{co}\sin\left(\frac{x-\alpha}{\omega\sqrt{LC}}\right) - \frac{V\omega C}{\omega^2LC-1}\cos(x) + \frac{V}{\omega^2LC-1}\left(\omega\,C\cos\left(\frac{x-\alpha}{\omega\sqrt{LC}}\right)\times\cos(\alpha) - \sqrt{\frac{C}{L}}\sin(\alpha)\sin\left(\frac{x-\alpha}{\omega\sqrt{LC}}\right)\right). \tag{6}$$

This equation incorporates initial conditions for the capacitor voltage (V_{co}) and inductor current (I_{Lo}), along with a phase shift (α) introduced to the external sinusoidal voltage at the beginning of the considered time period. The submodule capacitors of each arm of the MMC are maintained at close voltages from each other owing to the voltage balancing algorithm within each arm. In this case, V_{co} is the initial capacitor voltage of the lumped arm capacitor in Fig. 3 within a considered time period. The external sinusoidal voltage source at the dc link possesses an amplitude V, and frequency f in Hz or ω in rd/s. Its instantaneous phase angle is represented by $x = \omega t + \alpha_o$, where α_o signifies the phase offset between the modulating signal in (2) and the sinusoidal ripple present in the dc link. Equations (5) and (6) express the inverse Laplace transforms of the capacitor voltage and inductor current, respectively, derived from (4) while neglecting the series resistance. These equations define the capacitor voltages, denoted by $V_c(x)$ and $V_c'(x)$, for the upper and lower half-bridges as functions of the instantaneous phase angle (x) of the applied external voltage.

To account for damping effects, (23) and (24) serve as modified versions of (5) and (6). These modified equations are then employed numerically to obtain the values of inductor currents ($I_{L,k}$, $I'_{L,k}$) and capacitor voltages ($V_{c,k}$, $V'_{c,k}$) in Fig. 6.

In Fig. 5, the equivalent circuit operates by the half-bridge capacitors exchanging roles to establish a series R-L-C configuration every half-cycle of the fundamental period (T_s) of the high-frequency link. By analyzing (5) and (6) at the conclusion of each half-cycle, we arrive at (7)–(10). In (7)–(10), $V_{c,k-1}$ and $V'_{c,k-1}$ represent the capacitor voltages for the upper and lower half-bridges, respectively, at the initiation of their corresponding half-cycles within the kth cycle of the switching frequency waveform. Likewise, $I_{L,k-1}$ and $I'_{L,k-1}$ signify the inductor currents at the beginning of the first and second half-cycles in the kth cycle of the switching frequency waveform. These equations introduce the variable h, representing the portion of the external voltage's instantaneous phase angle covered within a $0.5\,T_s$ interval. Mathematically, h is expressed as $(\frac{0.5\,T_s}{T}\,2\pi)$, where T signifies the fundamental period of the externally applied voltage. In addition, α_{2k} denotes the angle traversed by the external voltage up to the beginning of the first half of the $(k+1)$th switching cycle. This value is calculated as $\alpha_o + 2kh$, where α_o is an initial angle and k represents an integer. Finally, the variable v appearing in these equations is defined in (13). When the submodule capacitances of either of the half-bridges is swapped out, its voltage does not change. For example, the voltage at the end of the first half of the kth cycle $V_c(\alpha_{2k-1})$, is identical to the voltage at the beginning of the first half of the $(k+1)^{th}$ cycle $V_c(\alpha_{2k})$, as illustrated in Fig. 6. This property ensures continuity of operation during capacitance swapping arising from insertion of HF-MMC upper and lower arm SMs in complementary half-cycles of switching frequency.

To model the terminal behavior of the two half-bridge controlled capacitors, the Fourier component of V_{mod} in Fig. 5, at the frequency of the driving voltage source is obtained. This is

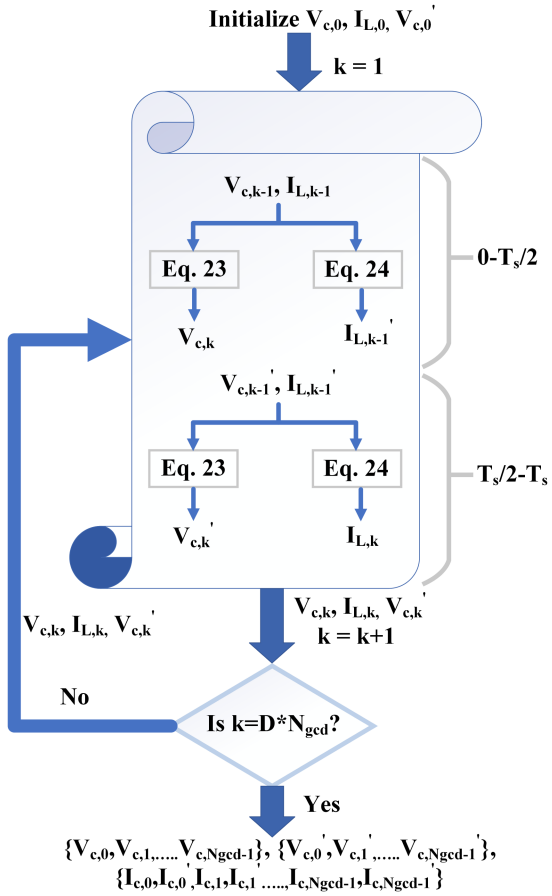

Fig. 6. Equations (23) and (24) (damped versions of (5) and (6)) are iterated N_{gcd} times to reach a period, when V_c and i_L return to their initial values. Convergence takes D iterations with an arbitrary initial guess for $V_c(0)$, $V_c'(0)$, and $I_L(0)$. (i) $I_L'(0) = i_L(T_s/2)$, $I_L(1) = i_L(T_s)$, $V_c(1) = V_c(T_s/2) = V_c(T_s)$ (upper capacitor bypassed during $Ts/2 - Ts$). (ii) $V_c'(1) = V_c'(T_s) = V_c'(T_s + T_s/2)$ (lower capacitor bypassed during T_s - T_s + $\frac{T_s}{2}$). After convergence (D iterations), the 2 N_{gcd} values of V_c and i_L are used in (12).

derived using expressions for $V_c(x)$ and $V_c'(x)$ from (5) in (11).

$$V_{c,k} = V_{c,k-1}\cos(v) + \sqrt{\frac{L}{C}} I_{L,k-1}\sin(v) - \frac{V}{\omega^2 LC - 1}\sin(\alpha_{2k-1}) + \frac{V}{\omega^2 LC - 1}\left(\cos(v)\sin(\alpha_{2k-2}) + \omega\sqrt{LC}\cos(\alpha_{2k-2})\sin(v)\right) \tag{7}$$

$$I_{L,k} = I_{L,k-1}'\cos(v) - \sqrt{\frac{C}{L}} V_{c,k-1}'\sin(v) - \frac{V\omega C}{\omega^2 LC - 1}\cos(\alpha_{2k}) + \frac{V}{\omega^2 LC - 1}\left(\omega C\cos(v)\cos(\alpha_{2k-1}) - \sqrt{\frac{C}{L}}\sin(\alpha_{2k-1})\sin(v)\right) \tag{8}$$

$$V_{c,k}' = V_{c,k-1}'\cos(v) + \sqrt{\frac{L}{C}} I_{L,k-1}'\sin(v) - \frac{V}{\omega^2 LC - 1}\sin(\alpha_{2k}) + \frac{V}{\omega^2 LC - 1}\left(\cos(v)\sin(\alpha_{2k-1}) + \omega\sqrt{LC}\cos(\alpha_{2k-1})\sin(v)\right) \tag{9}$$

$$I_{L,k-1}' = I_{L,k-1}\cos(v) - \sqrt{\frac{C}{L}} V_{c,k-1}\sin(v) - \frac{V\omega C}{\omega^2 LC - 1}\cos(\alpha_{2k-1}) + \frac{V}{\omega^2 LC - 1}\left(\omega C\cos(v)\cos(\alpha_{2k-2}) - \sqrt{\frac{C}{L}}\sin(\alpha_{2k-2})\sin(v)\right). \tag{10}$$

By hitting the upper and lower capacitor voltages given by (5), with $\cos(x)$ and $-j\sin(x)$ (so that the magnitude of the component at the frequency of external ripple can be obtained) in their respective half cycles, and taking the average over a period of each of the submodule's output voltage, (12) shown at the bottom of the next page is derived. The definition of various quantities in (12) is provided in (13).

$$V_{mod} = \frac{2}{N_f\,(2\pi)} \sum_{k=0}^{N_{gcd}-1} \left[\int_{\alpha_o + 2\,k\,h}^{\alpha_o + (2\,k+1)h} V_c(x) e^{-jx} dx + \int_{\alpha_o + (2\,k+1)h}^{\alpha_o + (2\,k+2)h} V_c'(x) e^{-jx} dx \right] \tag{11}$$

As shown for an example in Fig. 7, the capacitor voltages exhibit a periodic behavior with a period corresponding to N_{gcd} cycles of the switching frequency, f_s. Within this repetitive interval, the driving voltage completes N_f cycles, where the definitions of N_f and N_{gcd} are provided in (13). To facilitate integration, the total integral over this period is decomposed into N_{gcd} pairings of smaller integrals, each with a duration of h, as detailed in (11).

$$F_1 = \frac{A\,(\omega C)\,V}{\omega^2 LC - 1}, F_2 = \frac{B\,V}{\omega^2 LC - 1}, F_a = \frac{V}{\omega^2 LC - 1}$$
$$N_{gcd} = \frac{f_s}{GCD(f, f_s)}, N_f = \frac{f}{GCD(f, f_s)}$$
$$h = \frac{0.5\,T_s}{T} 2\pi = \frac{\pi N_f}{N_{gcd}}, v = \frac{0.5\,T_s}{\sqrt{LC}} \tag{13}$$

$$A = \left(\frac{e^{-j\alpha_o}\omega L}{(\omega^2 LC - 1)}\right) \left[-1 + e^{-j\,h}\left(\cos(v) + j\omega\sqrt{LC}\sin(v)\right)\right]$$
$$B = \left(\frac{e^{-j\alpha_o}\omega\sqrt{LC}}{\omega^2 LC - 1}\right) \left[-j\,\omega\sqrt{LC} - e^{-j\,h}\left(-j\omega\sqrt{LC}\cos(v) + \sin(v)\right)\right]. \tag{14}$$

TABLE I
RESONANT PEAKS IN THE FREQUENCY RESPONSE OF THE HF-MMC PHASE LEGS DESIGNED FOR VARIOUS FUNDAMENTAL LINK FREQUENCIES, f_s

$f_s(kHz)$	$L(\mu H)$ -$2L_{arm}$	$C(\mu F)$ -$0.25C_{sm}$	$\theta(rad)$ -Eq. (26)	$f_{SS,t}(kHz)$ -Eq. (36)	$f_{SS,o}(kHz)$ -Observed	$V_{mod}(V)$ -$f_{SS,t}$	$V_{mod}(V)$ -$f_{SS,o}$	DP(kHz)-Observed
10	57.7	7.96	2.8312	4.506	4.5	1960	1964	15.5, 24.5, 30
50	7.9	2.65	2.7055	21.529	21.3	1314	1324	79, 121.53 150
oh 1	400	62.5	3.1414	0.499	0.495	1137	1147	1.5, 2.5, -, 3.5
1	400	50	3.0650	0.4878	0.480	771.5	803.6	1.515, 2.495, 3, 3.520
1	400	37.5	2.7277	0.4341	0.425	382.6	427.2	1.565, 2.445, 3, 3.575
1	400	25	1.7478	0.2782	0.270	259.5	267.6	1.721, 2.290, 3, 3.730

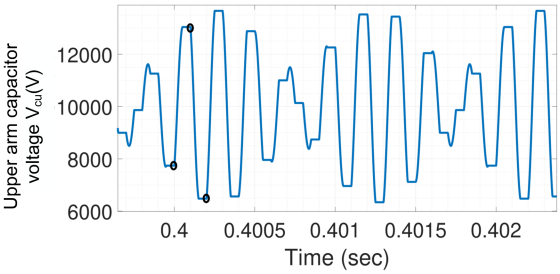

Fig. 7. Upper half-bridge capacitor voltage $V_c(t)$ in Fig. 5 for a DC side ripple voltage of 250 V at 4500 Hz—It takes $N_{gcd} = 20$ cycles of $f_s = 10$ kHz for a period of $V_c(t)$ to complete-, e.g., 0.4–0.402 s. The first three initial values $V_{c,k}$ for $k = 0, 1, 2$ out of a total of 20 within a period, starting from 0.4 s are marked as black ellipses.

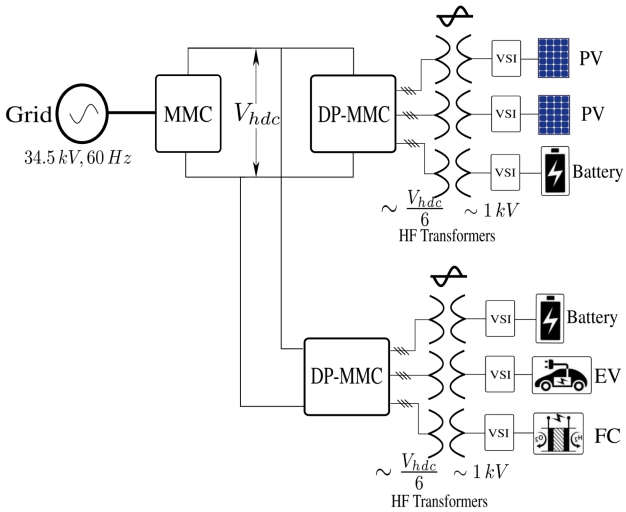

Fig. 8. Block diagram of the presented DP-MMC topology in a multiconverter configuration with a common dc link interfacing PV arrays, electric vehicle charging stations, storage units, and fuel cells.

The computation in (12) requires a total of $2\,N_{gcd}$ pairs of initial conditions: Capacitor voltages (V_c and V_c') and inductor currents (I_L and I_L'). These initial conditions are taken at the beginning of each half-cycle of f_s and span N_{gcd} cycles. Fig. 13(a)–(c) exemplifies this concept for $f = f_s = 10$ kHz. The waveforms demonstrate that V_c, V_c', and I_L complete a period after $N_{gcd} = 1$ cycle of f_s. Consequently, the corresponding capacitor voltages and inductor current at the start of the first and second half-cycles of f_s are required for the calculation. Similarly, Fig. 7 illustrates the case where $f = 4.5$ kHz and $f_s = 10$ kHz. Here, $N_{gcd} = 20$ (corresponding to 20 cycles of f_s) as $V_c(t)$ completes a period. The general numerical formulation for determining all initial conditions required for Fourier series component evaluation in (12) is presented in Fig. 6.

In (12), the term containing F_a represents the voltage component if both the half bridges were together replaced with a capacitor of value C_{sm}/N. This equivalence arises because $\frac{N_{gcd}\,h}{N_f\,\pi} = 1$. Consequently, the remaining portion of the term simplifies to $\frac{j\,V}{\omega^2\,LC-1}$, which is demonstrably the voltage across a capacitor in an L-C circuit stimulated by a sinusoidal voltage source.

A and B in (13) both go to zero under the following conditions:

$$f = 2\,p\,f_s, f_s = \frac{1}{2\pi\sqrt{LC}}\frac{1}{2q}, p, q\,\epsilon N$$
$$f \neq \frac{1}{2\pi\sqrt{LC}}. \tag{15}$$

For example, this means that if the resonant frequency formed by L_{arm} and C_{sm}/N is 20 kHz, then for $f_s = 10$ kHz and $f = 40$ kHz, the half-bridges behave like a simple capacitance of value C_{sm}/N.

In Fig. 11(a), the blue dotted line represents the magnitude response of the term F_a in (12) along with the complete frequency response including all the terms. It can be seen that at very low and very high frequencies of ripple relative to $\frac{1}{2\pi\sqrt{LC}}$, the two half-bridges asymptotically follow the response of a simple capacitance of value C_{sm}/N. Further interpretation of

$$V_{mod} = \frac{1}{N_f\pi}\left[F_a(j\,N_{gcd}\,h) + B\sum_{k=0}^{N_{gcd}-1}(V_{co,k} + V'_{co,k}e^{-jh})e^{-jk2h} + A\sum_{k=0}^{N_{gcd}-1}(I_{o,k} + I'_{o,k}e^{-jh})e^{-jk2h}\right.$$
$$\left. + \sum_{m=0}^{2N_{gcd}-1}\left(F_1\cos(\alpha_o + mh) + F_2\sin(\alpha_o + mh)\right)e^{-jmh}\right]. \tag{12}$$

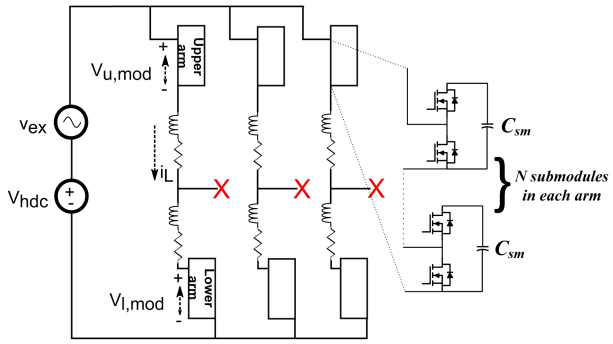

Fig. 9. HF-MMC circuit to compare time domain waveforms and frequency response of the HF-MMC phase legs.

(12) is deferred until after the investigation into the trend of the initial inductor current and capacitor voltages $V_{c,k}, V'_{c,k}$ and $I_{L,k}, I'_{L,k}$ of (12) which is provided next.

C. Initial Condition Analysis of State-Variables

In (12), the sum $(V_{co,k} + V'_{co,k}e^{-jh})$ and $(I_{o,k} + I'_{o,k}e^{-jh})$ involving the initial conditions of the inductor current and the capacitor voltages at the half-cycle boundaries significantly impact the frequency response of the modulated output voltage (V_{mod}) to the ripple voltages at the dc link. In particular, these sums blow up to huge values when certain conditions relating to the eigenvalues (26) of the initial condition vector matrix (16) are satisfied. These conditions are studied to extract the sensitive frequencies of ripple in this section. As an example, in Fig. 11(a), the magnitude of V_{mod} is plotted for various ripple frequencies. It is consistently observed that a peak occurs at the link frequency, which corresponds to the switching frequency of the two half-bridges, regardless of changes in circuit parameters. In addition, a resonant peak appears at a lower frequency. These two primary resonant peaks are designated as the invariant resonant frequency (IRF) and the variant resonant frequency (VRF) in this work. The subsequent resonant peaks observed in Fig. 11(a) at higher frequencies are referred to as follower resonant frequencies (FRF).

1) Matrix Formulation:

$$\underbrace{\begin{pmatrix} I_{L,1} \\ V_{c,1} \\ V'_{c,1} \end{pmatrix}}_{\mathrm{W_1}} = \underbrace{\begin{pmatrix} \cos^2(v) & -\frac{y}{2}\sin(2v) & -y\sin(v) \\ \frac{1}{y}\sin(v) & \cos(v) & 0 \\ \frac{1}{2y}\sin(2v) & -\sin^2(v) & \cos(v) \end{pmatrix}}_{\mathrm{P}} \underbrace{\begin{pmatrix} I_{L,o} \\ V_{c,o} \\ V'_{c,o} \end{pmatrix}}_{\mathrm{W_o}} + J_o$$

$$y = \sqrt{\frac{C}{L}} \tag{16}$$

$$\underbrace{\begin{pmatrix} I'_{L,1} \\ V'_{c,1} \\ V_{c,1} \end{pmatrix}}_{\mathrm{W'_1}} = P \underbrace{\begin{pmatrix} I'_{L,o} \\ V'_{c,o} \\ V_{c,o} \end{pmatrix}}_{\mathrm{W'_o}} + J_o e^{j\,h}. \tag{17}$$

The analysis begins by investigating the two dominant resonant peaks. To achieve this, a matrix formulation is derived in (16). This formulation expresses the initial state variables at the cycle's beginning as a function of their values at the preceding cycle's initiation (two half-cycles prior). The terms describing the influence of the externally applied voltage in (7)–(10) are represented by the term J_o in (16). Notably, matrix P stays constant throughout every cycle defined by the switching frequency f_s. It is important to consider that N_{gcd} cycles of this nature are required to complete a single period of the capacitor voltages or the inductor current. (17) builds upon this concept by formulating a similar matrix equation. However, the starting point in (17) is set to I'_{Lo} and V'_{co} as depicted in Fig. 6. Consequently, the external applied voltage functions incorporated in (7)–(10) are advanced by an angle h in (17). Since (12) contains the sum of the initial condition terms such as $V_{c,k} + V'_{c,k}e^{-j\,h}$, a new initial condition vector as shown in (18) is synthesized by adding (16), and (17) multiplied by $e^{-j\,h}$

$$U_n = W_n + W'_n e^{-jh},\ Q_n = 2J_n,\ n = 0, 1, 2\ldots$$
$$U_1 = P\,U_o + Q_o. \tag{18}$$

Equation (18) exhibits an interesting relationship, where $Q_n = 2\,J_n$. This translates to $W_n + W'_n\,e^{-jh}$ simplifying to just $2\,W_n$. This behavior is corroborated by simulations, where $I_{Ln} + I'_{Ln}\,e^{-jh} = 2\,I_{Ln}$ and $V_{cn} + V'_{cn}e^{-jh} = 2\,V_{cn}$ is observed. For instance, at $f = f_s$ where $h = \pi$, Fig. 13(b) and (c) visually confirm that $I_{L,0} + I'_{L,0}\,e^{-j\pi} = 2I_{L,0}$ and $V_{c,0} + V'_{c,0}\,e^{-j\pi} = 2V_{c,0}$. Using the same observation, it can be seen that differential mode content in the arm voltages due to the ripple in the dc link is zero as shown in (19). From (12), it can be seen that the terms containing F_a, F_1, and F_2 is equally distributed between upper and lower arms if the submodule capacitors in the arms are the same value and the terms containing A and B go to zero in the differential mode extraction as explained above (i.e., $W_n - W'_n\,e^{-jh} = 0$).

$$\underbrace{0}_{\mathrm{V_{mod,diff}}} = \frac{2}{N_f\,(2\pi)} \sum_{k=0}^{N_{gcd}-1} \left[\int_{\alpha_o+2\,k\,h}^{\alpha_o+(2\,k+1)h} V_c(x)e^{-jx}dx - \int_{\alpha_o+(2\,k+1)h}^{\alpha_o+(2\,k+2)h} V'_c(x)e^{-jx}dx \right]. \tag{19}$$

2) General Form for Initial Condition Vector: The general form for the vector U_n in (18) can be written as a series as shown in (20) and (21).

$$U_{n+1} = P\,U_n + Q_n = P\,(P\,U_{n-1} + Q_{n-1}) + Q_n$$
$$= P^2\,U_{n-1} + P\,Q_{n-1} + Q_n. \tag{20}$$

The system exhibits periodic behavior, with the initial conditions returning to their original values after a specific number of

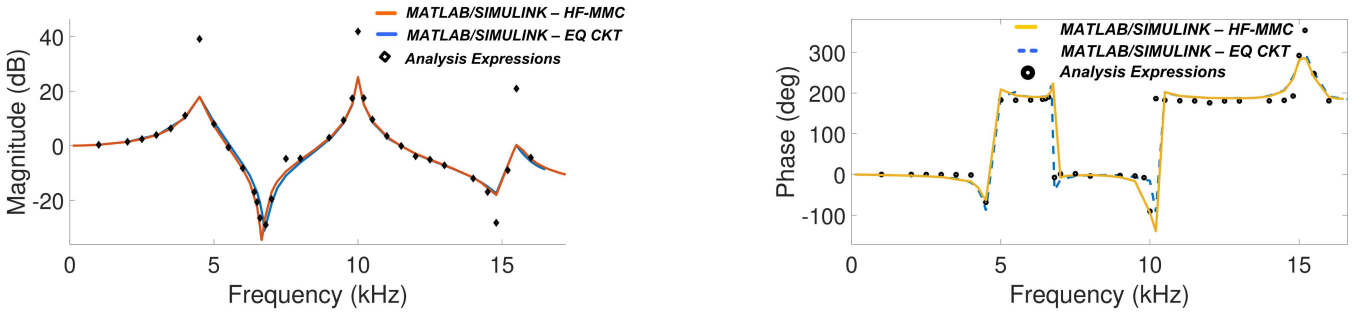

Fig. 10. (a) Magnitude versus frequency plot and (b) Phase versus frequency plot of V_{mod} at $f_s = 10$ kHz using circuit parameters from Table II with MATLAB/SIMULINK simulations of Figs. 9, 5 and calculated using (12) and Fig. 6.

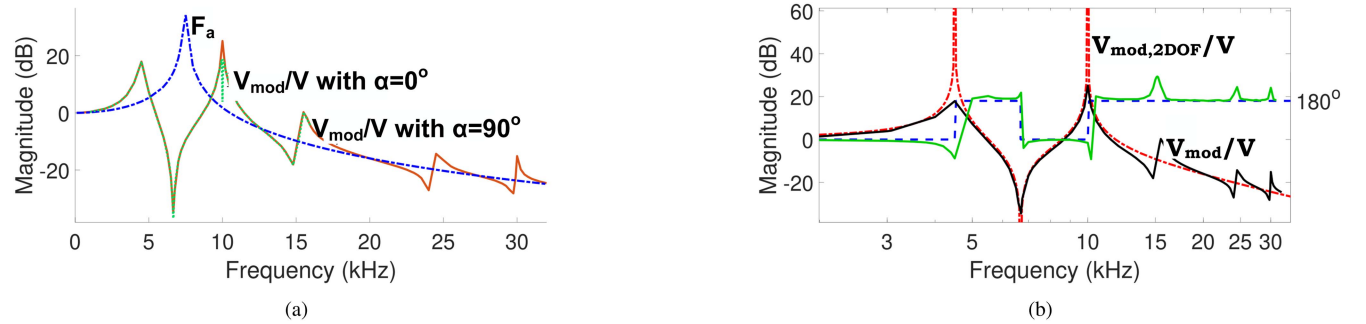

Fig. 11. Magnitude versus frequency plot of V_{mod} using circuit parameters from Table II and MATLAB/SIMULINK simulations. (a) With $\alpha_o = 0^o$ (green dotted line), with $\alpha_o = 90^o$ (red solid line), and of capacitor of value C_{sm}/N (blue dashed-dotted lines), (b) Comparison of magnitude and phase plot from (39) (red dashed-dotted and blue dotted lines) and from the equivalent circuit in Fig. 5 (black solid and green solid lines).

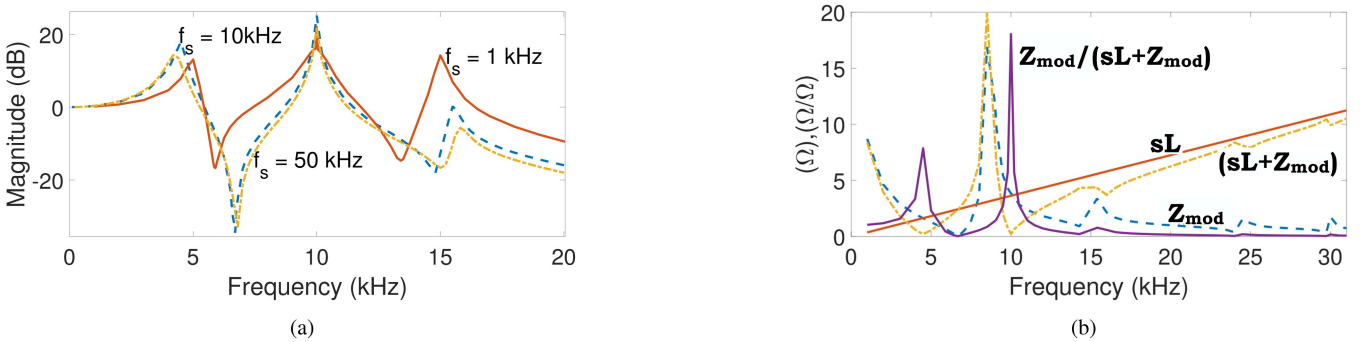

Fig. 12. Magnitude versus frequency plot of V_{mod} using circuit parameters from Table III and MATLAB/SIMULINK simulations. (a) At $f_s = 1$ kHz-solid line, 50 kHz-dashed-dotted line, with frequency axis scaled by 10 times and 0.2 times, respectively, and at $f_s = 10$ kHz-dotted line, (b) Effective impedance offered by the MMC submodules (blue dotted lines), the arm inductors (solid red line), the net impedance formed by the sum of the two (dashed-dotted yellow line) and the ratio $Z_{mod}/(Z_{mod} + s\,L)$(violet solid line) for $f_s = 10$ kHz from MATLAB/SIMULINK simulations.

cycles, denoted by $(n+1)$. This period is depicted in (21). $(n+1)$ is later set equal to N_{gcd}. As an illustration in Fig. 7, with $N_{gcd} = 20$, the initial voltage value at 0.4 s repeats again at 0.402 sec. at the beginning of the 21st cycle, signifying the completion of a period

$$U_o = U_{n+1} = P^{n+1}U_o + \underbrace{\sum_{i=0}^{n} P^i Q_{n-i}}_{\mathrm{R_n}}. \qquad (21)$$

Equation (21) defines a summation term, R_n, representing quantities dependent on the externally applied voltage. This term corresponds to the vector at the $(n+1)$th cycle, where n represents the maximum index of the summation.

3) Damping Factor and Characteristic Roots: The time-domain equations presented in (5) and (6) for RLC circuit analysis can be equivalently expressed as (22). In this form, $f_{\text{forced}}(t)$ represents the steady-state, forced response of the state variable. The remaining two terms constitute the circuit's natural

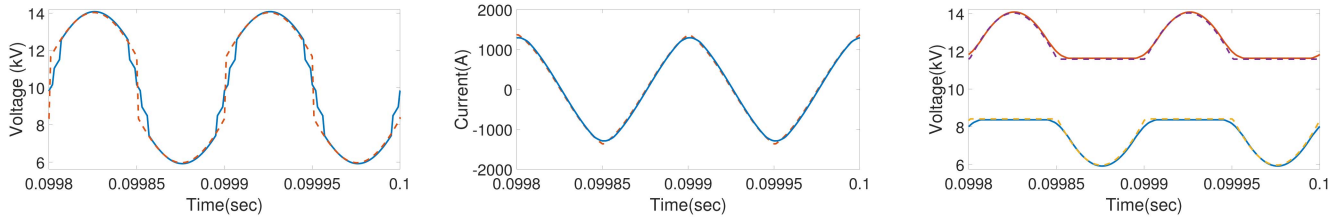

(a) (b) (c)

Fig. 13. Time domain waveforms from MATLAB/SIMULINK simulations at $f_s = 10$ kHz and circuit parameters in Table II showing (a) Sum of submodule output voltages from the HF-MMC (blue solid line) and from the equivalent circuit (orange dotted line), (b) Current drawn into each phase leg from the DC link of the HF-MMC (solid lines) and current in the equivalent circuit (dotted lines), (c) Sum of upper arm and lower arm submodule capacitor voltages in the HF-MMC (solid lines) and the capacitor voltages from the equivalent circuit(dotted lines).

response.

$$i_L = K_1\, e^{s_1\, t} + K_2\, e^{s_2\, t} + f_{\text{forced}}$$
$$s_1, s_2 = -\beta \pm \sqrt{\beta^2 - \omega_o^2}$$
$$\beta = \frac{R}{2\,L}, \omega_o = \frac{1}{\sqrt{LC}}. \tag{22}$$

For a system with minimal damping resistance ($R << \omega_o^2$), the characteristic roots (s_1 and s_2) approach $-\beta \pm j\omega_o$. By comparing these roots with the exponential terms $e^{\pm j\,\omega_o t}$ in (5) and (6), we observe the introduction of an additional damping factor, $r(t) = e^{\frac{-Rt}{2L}}$, in (23) and (24). This factor accounts for the exponential decay of the natural response over time, reflecting the influence of the small resistance (R)

$$V_c(x) = r(t)\, V_{co} \cos\left(\frac{t}{\sqrt{LC}}\right) + r(t)\sqrt{\frac{L}{C}}\, I_{Lo} \sin\left(\frac{t}{\sqrt{LC}}\right) - \frac{V}{\omega^2 LC - 1} \sin(\omega t + \alpha_o) + \frac{V\, r(t)}{\omega^2 LC - 1} \times \left(\cos\left(\frac{t}{\sqrt{LC}}\right) \sin(\alpha_o) + \omega\sqrt{LC} \cos(\alpha_o) \sin\left(\frac{t}{\sqrt{LC}}\right)\right) \tag{23}$$

$$i_L(x) = r(t)\, I_{Lo} \cos\left(\frac{t}{\sqrt{LC}}\right) - r(t)\sqrt{\frac{C}{L}}\, V_{co} \sin\left(\frac{t}{\sqrt{LC}}\right) - \frac{V\omega C}{\omega^2 LC - 1} \cos(\omega t + \alpha_o) + \frac{V\, r(t)}{\omega^2 LC - 1} \times \left(\omega\, C \cos\left(\frac{t}{\sqrt{LC}}\right) \cos(\alpha_o) - \sqrt{\frac{C}{L}} \sin(\alpha_o) \sin\left(\frac{t}{\sqrt{LC}}\right)\right). \tag{24}$$

Equation (25) introduces matrix P_R, which incorporates the damping factor $r(t)$ into (16), using (23) and (24) evaluated at the end of a half cycle ($t = 0.5\, T_s$).

$$P_R = r \begin{pmatrix} r\cos^2(v) & -r\frac{y}{2}\sin(2v) & -y\sin(v) \\ \frac{1}{y}\sin(v) & \cos(v) & 0 \\ \frac{r}{2y}\sin(2v) & -r\sin^2(v) & \cos(v) \end{pmatrix}$$

$$r = e^{-\frac{RT_s}{4L}}. \tag{25}$$

4) Diagonalization of Matrices and Eigenvalues: Equations in (26) address the diagonalization of matrices P and P_R. The characteristic equation of P in (27), determines its eigenvalues, represented by the diagonal elements of the matrix $\wedge$ in (26). While the exact eigenvalues of P_R are mathematically complex, the analysis approximates the r values within P_R elements to 1 using the condition $4L/R >> T_s$ for simplification.

$$P = T \wedge T^{-1}, P_R \simeq T \wedge_R T^{-1}$$
$$\wedge = \begin{pmatrix} 1 & & \\ & e^{j\theta} & \\ & & e^{-j\theta} \end{pmatrix}, \wedge_R = \begin{pmatrix} r & & \\ & r\, e^{j\theta} & \\ & & r\, e^{-j\theta} \end{pmatrix}$$
$$e^{\pm j\theta} = \frac{1}{4}\left[q \pm \sqrt{-16 + q^2}\right] \tag{26}$$
$$\left[2\lambda^2 - \underbrace{(\cos(2v) + 4\cos(v) - 1)}_{\text{q}}\,\lambda + 2\right](\lambda - 1) = 0. \tag{27}$$

The eigenvalues of the matrix P_R correspond to the elements of the $\wedge_R$ matrix presented in (26). It is crucial to recognize that θ is solely determined by the L and C values established previously. Equation (28) can be derived from (21) by substituting P_R for P and $R_{r,N_{gcd-1}}$ for R_n

$$U_o = (I_d - P_R^{N_{gcd}})^{-1} R_{r,N_{gcd}-1}. \tag{28}$$

5) Deriving the Expression for Uk: We can further express $R_{r,N_{gcd-1}}$ by leveraging the fact that the eigenvectors of P_R constitute a basis for $\mathbb{R}^3$. This allows us to represent U_o as depicted as follows:

$$U_o = \gamma_1 (I_d - P_R^{N_{gcd}})^{-1} E_1 + \gamma_2 (I_d - P_R^{N_{gcd}})^{-1} E_2 + \gamma_3 (I_d - P_R^{N_{gcd}})^{-1} E_3$$
$$U_o = \gamma_1 \frac{1}{1 - (r)^{N_{gcd}}} E_1 + \gamma_2 \frac{1}{1 - (r\, e^{j\theta})^{N_{gcd}}} E_2 + \gamma_3 \frac{1}{1 - (r\, e^{-j\theta})^{N_{gcd}}} E_3. \tag{29}$$

Here, the magnitudes of $R_{r,N_{gcd-1}}$ along the eigenvector directions are denoted as γ_1, γ_2, and γ_3. While analytical expressions for these γ values are not available, the structure of U_k still offers valuable insights, as demonstrated below. Furthermore, the magnitude response at any given frequency can still be determined numerically. This is achieved by employing the iterative formulation outlined in Fig. 6 to calculate initial values for the capacitor voltages and inductor currents, which are then incorporated into (12).

It can be demonstrated that the expression for U_k in (30) follows from the substitution of the equation for U_o in (29) and using the general form for U_n in (21).

$$U_k = \gamma_1 \frac{r^k}{1-(r)^{N_{gcd}}} E_1 + \gamma_2 \frac{r^k\, e^{jk\theta}}{1-(r\, e^{j\theta})^{N_{gcd}}} E_2 \\ \gamma_3 \frac{r^k\, e^{-jk\theta}}{1-(r\, e^{-j\theta})^{N_{gcd}}} E_3 + R_{r,k-1}. \tag{30}$$

6) Evaluating the Summation in (12) Using U_k: Leveraging the expression for U_k derived in (30), the summation in (12) can be evaluated for the first two terms of U_k. This yields (31) and (32) by virtue of the well-known formula for the sum of a geometric series. Furthermore, recognizing that $2h = \frac{T_s}{T} 2\pi$, and employing the substitutions $N_{gcd} = \frac{f_s}{GCD(f,f_s)}$ and $N_f = \frac{f}{GCD(f,fs)}$, we arrive at the expression $2h = \frac{2\pi N_f}{N_{gcd}}$ which is used to write (32)

$$\frac{\gamma_1 E_1}{1-(r)^{N_{gcd}}} \sum_{k=0}^{N_{gcd}-1} r^k e^{-jk2h} = \begin{cases} \frac{\gamma_1 E_1}{1-r}, f = nf_s, n\,\epsilon\,\mathbb{N} \\ \frac{\gamma_1 E_1}{1-r\, e^{-j\frac{2\pi N_f}{N_{gcd}}}}, \text{otherwise} \end{cases} \tag{31}$$

$$\frac{\gamma_2 E_2}{1-(re^{j\theta})^{N_{gcd}}} \sum_{k=0}^{N_{gcd}-1} r^k\, e^{jk(\theta-2h)} \\ = \begin{cases} \frac{\gamma_2 E_2}{1-r}, \theta = 2\,h \text{ or } \Delta = n\,2\pi, n\,\epsilon\,\mathbb{N} \\ \frac{\gamma_2 E_2}{1-r\,e^{j\Delta}}, \Delta \neq m\,2\pi, \theta N_{gcd} = m\,2\pi, m\,\epsilon\,\mathbb{Z} \\ \frac{\gamma_2 E_2}{1-(re^{j\theta})^{N_{gcd}}} \left(\frac{1-(r\,e^{j\Delta})^{N_{gcd}}}{1-r\,e^{j\Delta}}\right), \text{otherwise} \end{cases} \\ \Delta = \theta - 2\,h \tag{32}$$

7) Invariant Resonant Frequency (IRF): According to (31), as r approaches 1, the sum of the U_k terms in (12) converges to a large value at the frequency $f = nf_s$. At this specific frequency, N_f is equal to nN_{gcd}. It is important to note that for $f = n\,f_s$, N_{gcd} becomes 1. For instance, if $f_s = 10$ kHz and $f = 30$ kHz, then $N_{gcd} = 1$ and $N_f = 3$. The first case presented in (31) can be understood as a special case of the more general formula in the second case, obtained by setting $N_f = nN_{gcd}$.

This reveals that for frequencies corresponding to multiples of f_s, especially, odd multiples of f_s, a peak response is observed as expressed in (37). Notably, the peak at $f = f_s$ is the most significant because for other odd multiples, the term $\omega^2\, LC - 1$ in the denominator becomes significantly larger when ω is much greater than $\frac{1}{\sqrt{LC}}$. Consequently, the invariant resonant peak occurs at the frequency, f_{IRF}, specified as follows:

$$f_{IRF} = f_s. \tag{34}$$

The expressions for the initial condition values of current through the inductor, $I_{L,0}$, and voltage across the capacitor, $V_{c,0}$, are given by (33) shown at the bottom of the next page for the case of $N_{gcd} = 1$ and $f = nf_s$. As described previously in (17) and (18), $I'_{L,0}$ and $V'_{c,0}$ are the negative of these values.

8) Analysis of Even Multiples of f_s and α_o: Equation (33) indicates that for frequencies corresponding to even multiples of f_s, the resonant peak is absent. This is attributed to the influence of the parameter γ_1, which also affects the magnitude of U_k as previously discussed. Furthermore, (33) indicates that when α_o equals zero, the magnitudes of both $I_{L,0}$ and $V_{c,0}$ are negligible. Fig. 11(a) illustrates the magnitude response of V_{mod} for α_o set to 0^o overlayed with case for $\alpha_o = 90^o$ and a switching frequency f_s of 10 kHz. While a sharp notch is observed at f_s for $\alpha_o = 0^o$, the magnitude exhibits significant peaking at frequencies very close to f_s, similar to the case with α_o set to 90^o.

9) Invariance of IRF Peak With Circuit Parameter Variation: This study reveals an intriguing characteristic—the resonant peak observed at frequency f_{IRF} exhibits negligible sensitivity to variations in component values L and C. However, the permissible increase in L that maintains the IRF peak is demonstrably dependent on the dc link voltage, V_{hdc} (as illustrated in Fig. 5). A significant value of modulation voltage, V_{mod}, at the switching frequency, f_s, arises due to the observed splitting of upper and lower half-bridge capacitor voltages [depicted in Fig. 13(c)]. In the extreme case, the voltage across the lower capacitor approaches zero. To achieve resonance at f_s, the terminal model of the half-bridges must present an impedance, Z_{mod}, equal to $-sL$ (where s is the Laplace variable). This condition is demonstrably satisfied at $f = f_s$ when $V_{mod} >> V$ and under the assumption of $R << sL$ [derived from (35) and corroborated by Fig. 12(b)]. At high values of L, the voltage split across the two capacitors becomes insufficient to replicate the voltage drop across sL while permitting a current limited solely by the circuit's resistance

$$Z_{mod} = \frac{R\left(\frac{sL}{R}+1\right)}{\frac{V}{V_{mod}}-1}. \tag{35}$$

$$I_{L,0} = \frac{V}{\omega^2 LC-1}\left(-\omega\, C\cos(\alpha_o) - \frac{2\,r}{r^2-1}\sqrt{\frac{C}{L}}\sin(\alpha_o)\sin(v)\right)\Bigg|_{\omega=(2n+1)\omega_s} \qquad I_{L,0} = \frac{-V\omega C\cos(\alpha_o)}{\omega^2 LC-1}\Bigg|_{\omega=(2n)\omega_s} \\ V_{c,0} = \frac{-V}{\omega^2 LC-1}\frac{1+r^2+2\,r\cos(v)}{r^2-1}\sin(\alpha_o)\Bigg|_{\omega=(2n+1)\omega_s} \qquad V_{c,0} = \frac{-V\sin(\alpha_o)}{\omega^2 LC-1}\Bigg|_{\omega=(2n)\omega_s}. \tag{33}$$

10) Variant Resonant Frequency (VRF): In a similar vein to (31), (32) suggests that the summation of terms denoted by U_k in (12) diverges towards a significantly large value when θ reaches $2h$. θ represents the angle of the complex conjugate eigenvalues pertaining to matrix P or P_R. This implies that resonance arises at the specific frequency denoted by f_{VRF} as follows:

$$f_{VRF} = \frac{\theta f_s}{2\pi}. \tag{36}$$

In (32), a general formula is established in case 3. This formula can be adapted to retrieve cases 1 and 2 by incorporating the specified conditions within the equation itself. To illustrate, consider a scenario where the sampling frequency, f_s, is set at 10 kHz. When the L and C values are those outlined in row I of Table I, (26) yields $\theta \simeq \frac{9}{20}2\pi$. Furthermore, (13) indicates that $2\,h$ is also $\frac{9}{20}2\pi$ at a frequency of $f = 4500$ Hz. Consequently, this leads to $\Delta = 0$ and the first case of (32). As a result, (36) confirms that $f_{VRF} = 4500$ Hz for the given arm inductance, submodule capacitance, and HF-link frequency values. It is noteworthy that for these specific L and C values and a frequency of $f = 4500Hz$, the term outside the summation on the left-hand side of (32) satisfies $\theta\, N_{gcd} = 2\pi$. Even for other frequencies such as 500 Hz,1500 Hz, 3500 Hz, etc., $N_{gcd} = 20$, (ΔN_{gcd}), and (θN_{gcd}) are multiples of 2π, but this only results in case 2 in (32). Only for $\Delta = 0$ or $\Delta = n2\pi$, case 1 holds. Note that $\theta N_{gcd} = 2\pi$ is automatically satisfied for $\theta = 2\,h$ in case 1 of (32).

11) Follower Resonant Frequencies (FRF): The magnitude response plot in Fig. 11(a) reveals additional resonant peaks beyond the initial two dominant peaks, observed at higher frequencies. These FRF peaks arise when the equation $2nf_s - f = \pm f_{IRF}$ or $2nf_s - f = \pm f_{VRF}$ is satisfied, where f_s represents the switching frequency, f denotes the external driving ripple frequency as illustrated as follows:

$$f_{FRF} = (2\,n\,f_s \pm f_{IRF,VRF})\,,\; n \epsilon \mathbb{N}. \tag{37}$$

This can be explained as follows: Using $\theta = \frac{2\pi T_s}{T_{ss}}$ from (36), the time period of the follower resonant frequency cycle, $T_{FRF} = \frac{1}{2nf_s + f_{VRF}}$ and $2h = \frac{2\pi T_s}{T_{FRF}}$, we get $\Delta = \theta - 2h$ to be a multiple of 2π and case 1 of (32) holds. A similar result can be obtained from the third term of U_k in (30) when $\Delta' = \theta + 2\,h$ becomes a multiple of 2π for $T_{FRF} = \frac{1}{2nf_s - f_{VRF}}$. The general condition on the ripple voltage frequency for Δ or Δ' to be a multiple of $2\,\pi$ is given as follows:

$$f_\Delta = pf_s \pm f_{VRF}, p \epsilon \mathbb{N}. \tag{38}$$

It is observed from the numerical calculation of initial conditions using Fig. 6 and (12) that there is an actual observed peak only for even values of p in (38) and this is captured in (37).

12) Comparison With Two-Degree-of-Freedom Model: It is observed that the two-degree-of-freedom model presented in (39) mimics the behavior of the model in (12), as illustrated in Fig. 11(b). The parameters d_1 and d_2 are determined by leveraging the magnitudes of V_{mod}, M_1, and M_2 at the resonant frequencies ω_{IRF} and ω_{VRF} obtained from (12) and Fig. 6, while ensuring a unity dc gain.

$$\frac{V_{mod,2DOF}}{V} = \frac{d_1\,(\omega_{IRF}^2)}{s^2 + \omega_{IRF}^2} + \frac{d_2\,(\omega_{VRF}^2)}{s^2 + \omega_{VRF}^2}$$
$$\frac{d_1\,(\omega_{IRF}^2)}{d_2\,(\omega_{VRF}^2)} = \frac{M_1}{M_2}$$
$$d_1 + d_2 = 1. \tag{39}$$

IV. Application of the HF-MMC Resonant Analysis

The presented analysis and mathematical framework can be leveraged to design the PWM schemes and switching frequencies of multiple MMCs back-to-back connected to a common dc link as shown in Fig. 8 [24]. The modulation schemes designed using the support of this analysis will ensure that the various resonances in the DP-MMCs in Fig. 8 are not excited.

Further, the phenomenon of the invariant resonant frequency can be taken advantage of, in designing a new power converter like the CLLLC [38], where the converter gain varies depending on the switching frequency. In this regard, there is a special advantage of the invariant resonant peak, that the circuit parameters can be designed at two-three times smaller values while keeping the resonant frequency fixed.

Yet another application of the presented analysis is in wireless power transfer and RF systems [35], [36] where the circuit resonant frequency changes with orientation changes between the power transfer coils. The invariant resonant frequency peak by its property of not changing with leakage inductance can once again be put to use in these applications.

V. Results–Matlab/Simulink

A. Agreement Between Theory and Experiment

In this study, we observed a high degree of agreement between theoretical predictions and experimental results. In Table I, the resonant peak frequencies are presented. In addition, expected values of f_{VRF} calculated using (36) and the angle of the complex pair of eigenvalues determined from (26) are tabulated for various HF-link frequencies, submodule capacitances, and arm inductance values. The IRF peak always occurs at the link frequency and is not separately tabulated in Table I.

The measured frequencies of the VRF peak and the FRF peaks (as shown in (37), (36) and Table I) deviated from theoretical values by a maximum of 2%. Similarly, the observed magnitude of V_{mod} at the theoretically predicted and experimentally determined f_{VRF} values differed by no more than 4%. For example, the first FRF peak in the last three rows of Table I at 1512.2 Hz, 1565.9 Hz, and 1721.8 Hz correspond to the tabulated f_{VRF} values, as predicted by (37).

B. Follower Resonant Frequencies (FRF)

Notably, the follower peaks of the IRF peak consistently appeared at odd multiples of the link frequencies (as described in (37)) when the dc link ripple was applied. The presence of a dominant FRF peak at times times the switching frequency

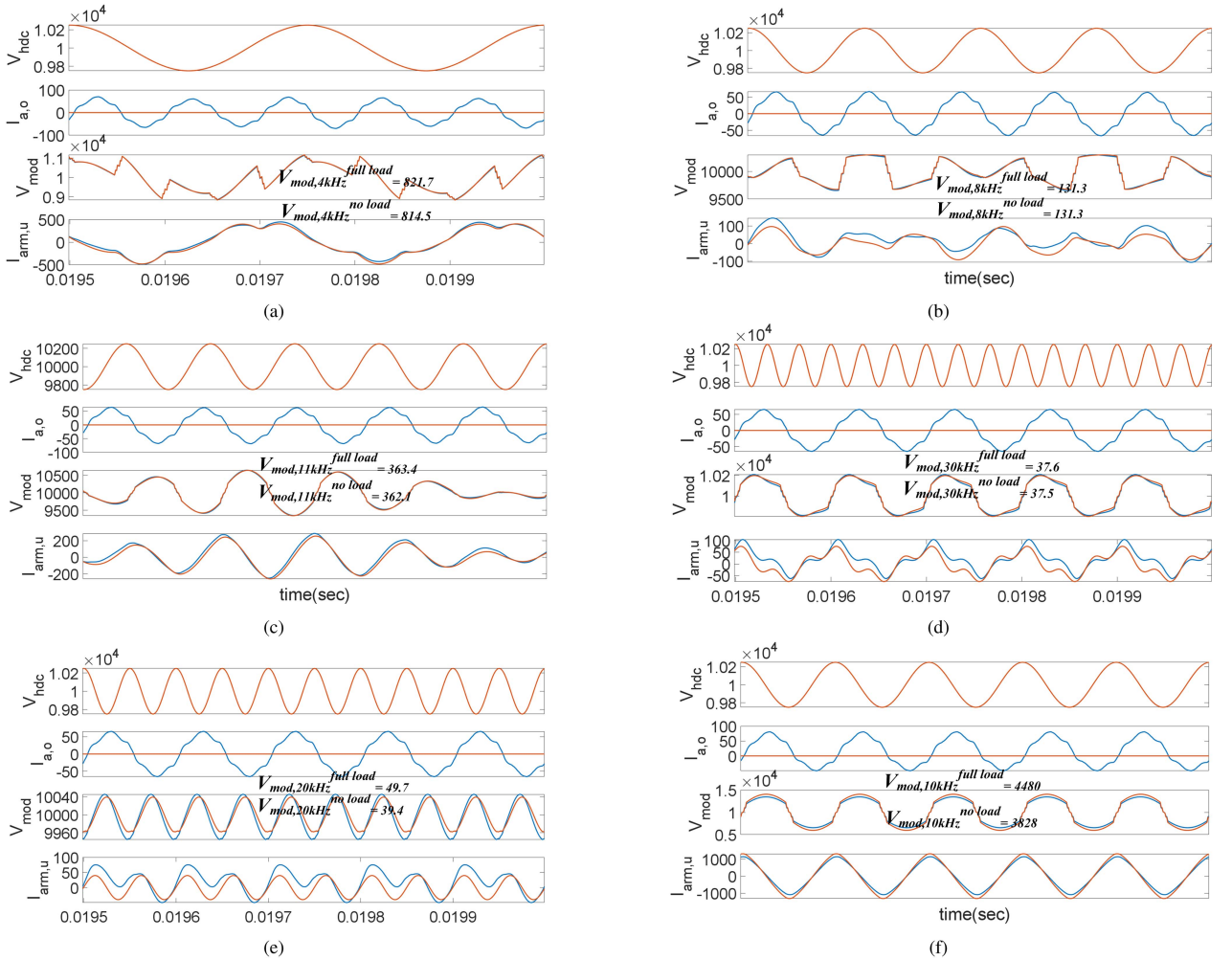

Fig. 14. Time domain waveforms from MATLAB/SIMULINK simulations using circuit parameters in Table II showing: HF-MMC DC link voltage ripple, output AC port currents, sum of submodule voltages in upper and lower arms, i.e., V_{mod} and arm currents plotted with rated output power flow (blue) overlayed with results from AC port disconnection (orange) for HF-link frequency of 10 kHz and DC link ripple frequency of (a) 4 kHz; (b) 8 kHz; (c) 11 kHz; (d) 30 kHz; (e) 20 kHz; (f) 10 kHz.

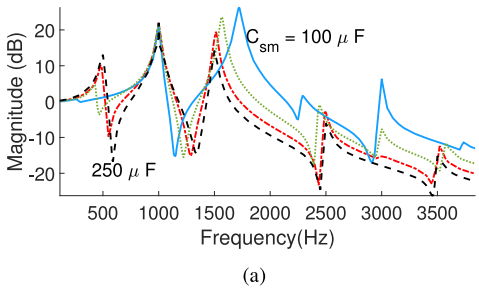

(a)

Fig. 15. (a) Magnitude response plot of V_{mod} for the link frequency of 1 kHz and $C_{sm} = 100$ μF (solid blue line), 150 μF (green dotted line), 200 μF (red dotted line) and 250 μF (black dashed line) with $L_{arm} = 200$ μH from MATLAB/SIMULINK simulations. The peaks in the plot have been tabulated in Table I.

$(3f_s)$ is observed in Fig. 15 for various values of the submodule capacitance (C_{sm}).

It is interesting to observe that the expected follower resonant peak at 3 kHz(row 3 of Table I) for a submodule capacitance value of $C_{sm} = 250$ μF is absent for the HF link at 1 kHz as tabulated in Table I and observed in Fig. 15. This can be explained by observing that the resonant frequency formed by the $2L_{arm}$ and $0.25\,C_{sm}$ for $C_{sm} = 250\mu F$ and $L_{arm} = 200$ μH is at the HF link frequency of 1 kHz. Substituting for $T_s = 2\pi\sqrt{LC}$ in v of (33) and $\omega = 3\omega_s$, reveals that the numerators of the terms dependent on r in $I_{L,0}$ and $V_{c,0}$ are almost zero in case the HF-link is at the resonant frequency. However, even in this case, the BS peak still exists because the denominator of these terms tend to zero faster than the numerator.

C. VRF Peak Diminishes

It is further noted that the magnitude of the VRF peak diminishes with decreasing C_{sm} values. This phenomenon can be attributed to the minimal amplification of U_k terms in (12) at VRF frequencies far away from the $L-C$ resonant frequency. This limited amplification occurs because the numerator of coefficients A and B in (14) is negligible at these frequencies.

TABLE II
NOMINAL PARAMETERS FOR THE CIRCUIT IN FIG. 9 USED TO COMPARE THE ANALYSIS RESULTS ON MATLAB/SIMULINK, OPAL-RT HIL, AND EXPERIMENTAL HW SETUPS

Parameter	MATLAB SIMULINK	OPAL-RT HIL	Experimental HW setup
V_{hdc}	10 kV	10kV	20 V
V_{ex}	250 V	250 V	2.5 V
HF-MMC switching frequency	10 kHz	1kHz	236 Hz
HF-MMC L_{arm}	$28.85\mu H$	$200\mu H$	$1.25mH$
HF-MMC C_{sm}	$31.83\mu F$	$250\mu F$	$80\mu F$
HF-MMC SMs per arm(N)	4	4	1

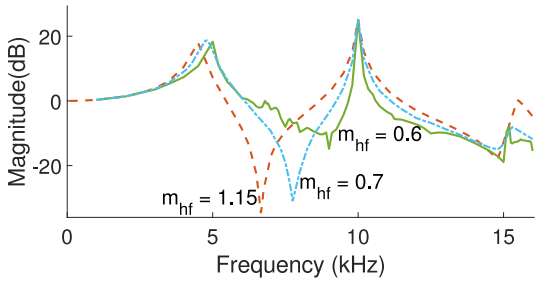

Fig. 16. Magnitude versus frequency plot of V_{mod} using circuit parameters from Table II from MATLAB/SIMULINK simulations for varying values of modulation index.

Consequently, as illustrated in Fig. 15, the corresponding FRF peaks exhibit a more significant amplitude in such scenarios.

D. Validation of Fourier Series Expression for V_{mod}

In Fig. 13(a), (b), and (c) are shown the time domain waveforms from the MATLAB/SIMULINK simulation of HF-MMC circuit and the equivalent circuit in Fig. 5 with a modulation index of $m_{hf} = 1.15$. These waveforms have been obtained for a 10 kHz HF link with circuit parameters as in Table II. It can be observed that the waveforms almost overlap with each other showing the validity of the equivalent circuit for high modulation indices.

The magnitude and phase plots of V_{mod} from the analysis, the equivalent circuit and the HF-MMC circuit extracted from Figs. 5 and 9 for a HF link frequency of 10 kHz and circuit parameters as in Table II, are shown in Fig. 10. The frequency response from the simulation and those from the analysis are observed to match well with each other. At close to resonant frequency of $\frac{1}{\sqrt{LC}}$ and at the two major resonant peak frequencies, there is an error from the experimental results in Fig. 10(a) due to (12) not considering the series resistance. It is interesting to note that the phase of V_{mod} in Fig. 10(b) alternates between almost 0^o and almost 180^o every time a resonant frequency is crossed. This can be understood from the general partial fraction expansion form such as in (39) for a multiresonant system [39].

E. Modulation Index Impact

In Fig. 16 are shown, the magnitude response plots from Fig. 9 for $m_{hf} = 0.7$, $m_{hf} = 0.6$, and $m_{hf} = 1.15$. It is seen that

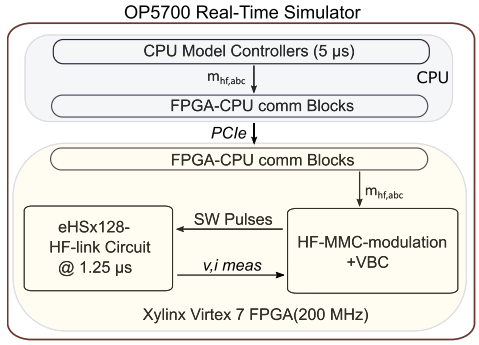

Fig. 17. Block diagram showing the functions performed by the subsystems of OP5700 real-time simulator.

TABLE III
PARAMETERS FOR EXTENDED SIMULATION IN MATLAB/SIMULINK BASED ON FIG. 9

Parameter	Value
V_{hdc}	10 kV
V_{ex}	250 V
MMC-L_{arm}, R_{arm},C_{sm}	1 kHz - 200 μH, 0.1 Ω, 250 μF 10 kHz - 28.847 μH, 0.1 Ω, 31.831 μF 50 kHz - 3.988 μH, 0.1 Ω, 10.61 μF

the VRF peak shifts slightly to the right while the IRF peak remains at the link frequency of f_s. Also, there are a number of microresonances occurring between the IRF and the VRF peaks as seen from the green solid line for lower modulation index of 0.6. Although at lower modulation indices such as 0.6 the total number of modules inserted per phase leg is still N, they are composed of (N-1) in one of the arms and 1 in the other for most of the time as against N and 0 for higher modulation indices. At these lower modulation indices, the requirement for all the N submodules to be inserted during a particular half-cycle of HF-link frequency does not arise and so the effective capacitance of the half-bridge in the equivalent circuit cannot be assumed to be C_{sm}/N. The capacitor voltages of these (N-1) capacitors in one arm and 1 capacitor in the other arm are balanced in two different groups they cannot be considered as a single capacitor anymore.

F. HF Link Frequency Dependence

In Fig. 12(a), the magnitude responses of Fig. 5 at HF link frequencies of 10 kHz, 1 kHz, and 50 kHz for C_{sm} and L_{arm} as tabulated in Table III are shown. The frequency axis for the 1-kHz plot has been scaled by ten times and that of the 50-kHz plot has been scaled by 0.2 times to show in the same plot. The VRF peak frequencies follow the expression obtained from the analysis as seen from Table I and the IRF peak remains fixed at the link frequency.

G. AC Port Decoupling for the Analysis

In Fig. 14, the time domain waveforms of V_{mod}, arm voltages, arm currents, and output port ac currents with rated power flow through the ac port and with ac port disconnected are shown.

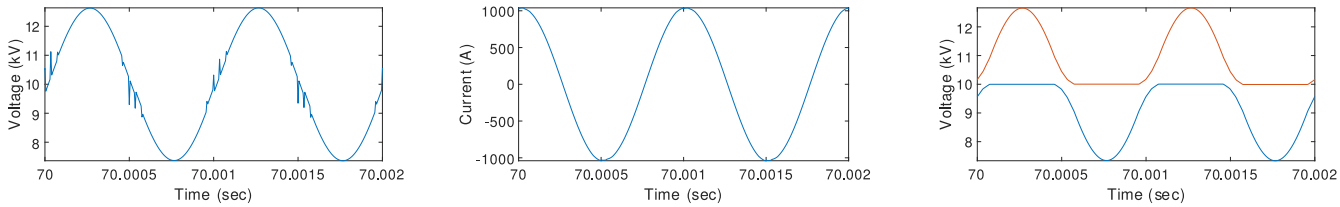

Fig. 18. Time domain waveforms from OPAL-RT real-time simulations of the HF-MMC circuit in Fig. 9,circuit parameters in Table II at DC link excitation frequency of 1 kHz showing: (a) Sum of submodule output voltages, (b) Current drawn into each phase leg from the DC link, (c) Sum of upper arm and lower arm submodule capacitor voltages.

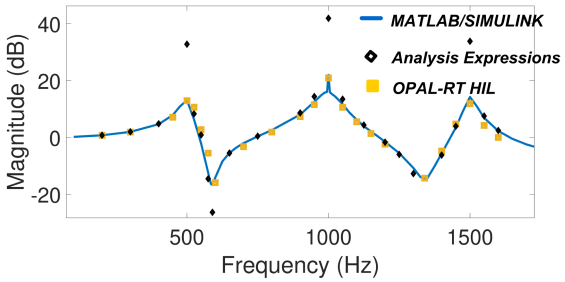

Fig. 19. OPAL-RT HIL real-time simulations of Fig. 9 (yellow squares) overlayed with results using analysis expressions (black diamonds) and corresponding MATLAB/SIMULINK simulations (blue solid line).

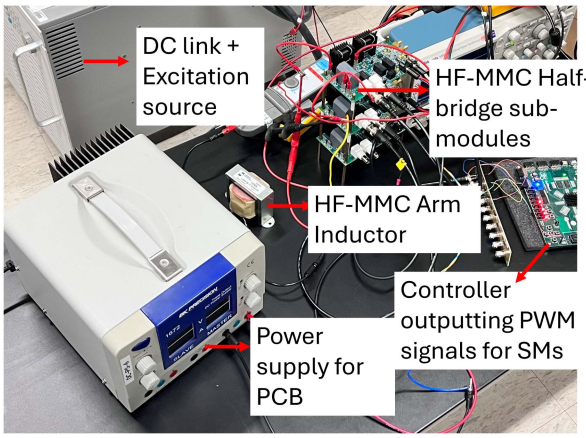

Fig. 20. Experimental hardware setup to evaluate dc side frequency response of the HF-MMC phase legs.

It can be observed that the response voltage V_{mod} (sum of the upper arm and lower arm submodule output voltages) to a ripple voltage at the dc link is not significantly changed as a result of output port ac currents. However, the submodule capacitor voltage ripple due to ac port currents and related $2f_{sw}$ voltage ripple do change but affect the magnitude of V_{mod} only slightly. It can be seen that at f_{sw} and even/odd harmonic frequencies of f_{sw}, there is a small difference in V_{mod} time-domain waveforms with ac port disconnected compared to rated power flow through the ac port connected. Since, the submodule capacitor values are designed to carry a small percentage of the ripple during regular operation, and the analysis targets characterizing the response V_{mod} due to a ripple in the dc link, these effects have been neglected in the analysis.

H. Comparison With Dual-Resonant Simplification

In the magnitude response plots, it has been repeatedly observed that there is an antiresonant dip between any two resonant peaks. This can again be explained as following from the partial fraction expansion form for a general multiresonant system such as shown in (39) [39]. If the coefficients d_1 and d_2 are of the same sign then there is an antiresonant dip between ω_{IRF} and ω_{VRF} since the denominators are of opposite sign at a frequency between the two resonant frequencies. In Fig. 11(b), the comparison of the magnitude response from (39) and from the equivalent circuit in Fig. 5 for $f_s = 10$ kHz is shown.

VI. Results—OPAL-RT Hardware-in-Loop and Experimental Hardware Setup

A. OPAL-RT Hardware-in-Loop Results

In Fig. 17, the block diagram of the HIL implementation on OPAL-RT for verification of the presented model is shown. Voltage balancing of the submodule capacitors and switching pulses for the HF-MMC are generated by custom created FPGA logic block. The switched model of the MMC circuit in Fig. 9 is implemented on the electrical Hardware Solver Block on the FPGA. The modulating signals for the HF-MMC are sent to the FPGA from the CPU cores in OPAL-RT. The time domain waveforms for a HF-link frequency of 1 kHz using circuit parameters as in Table II, obtained from OPAL-RT HIL real-time simulations are shown in Fig. 18(a), (b), and (c) and a similar trend can be observed.

The HF-link frequency has been chosen as 1 kHz and the corresponding circuit parameters are shown in Table II. The HF-link frequency has been reduced from 10 kHz which was used in MATLAB/SIMULINK so that the eHS solver with a solver time step of 1.25 μs can perform the modeling and simulation with good fidelity. The magnitude plots of the sum of upper arm and lower arm submodule output voltages in Fig. 9, from OPAL-RT based HIL simulation are shown in Fig. 19 for $m_{hf} = 1.15$. In the same figure, the magnitude plot of V_{mod} using the analytical expression in (12) and MATLAB/SIMULINK simulations of Fig. 5 are shown. Once again, a good match is observed between the three plots.

B. Experimental Hardware Results

The hardware experimental setup consists of two half-bridge modules, one for each arm of the HF-MMC phase leg as shown

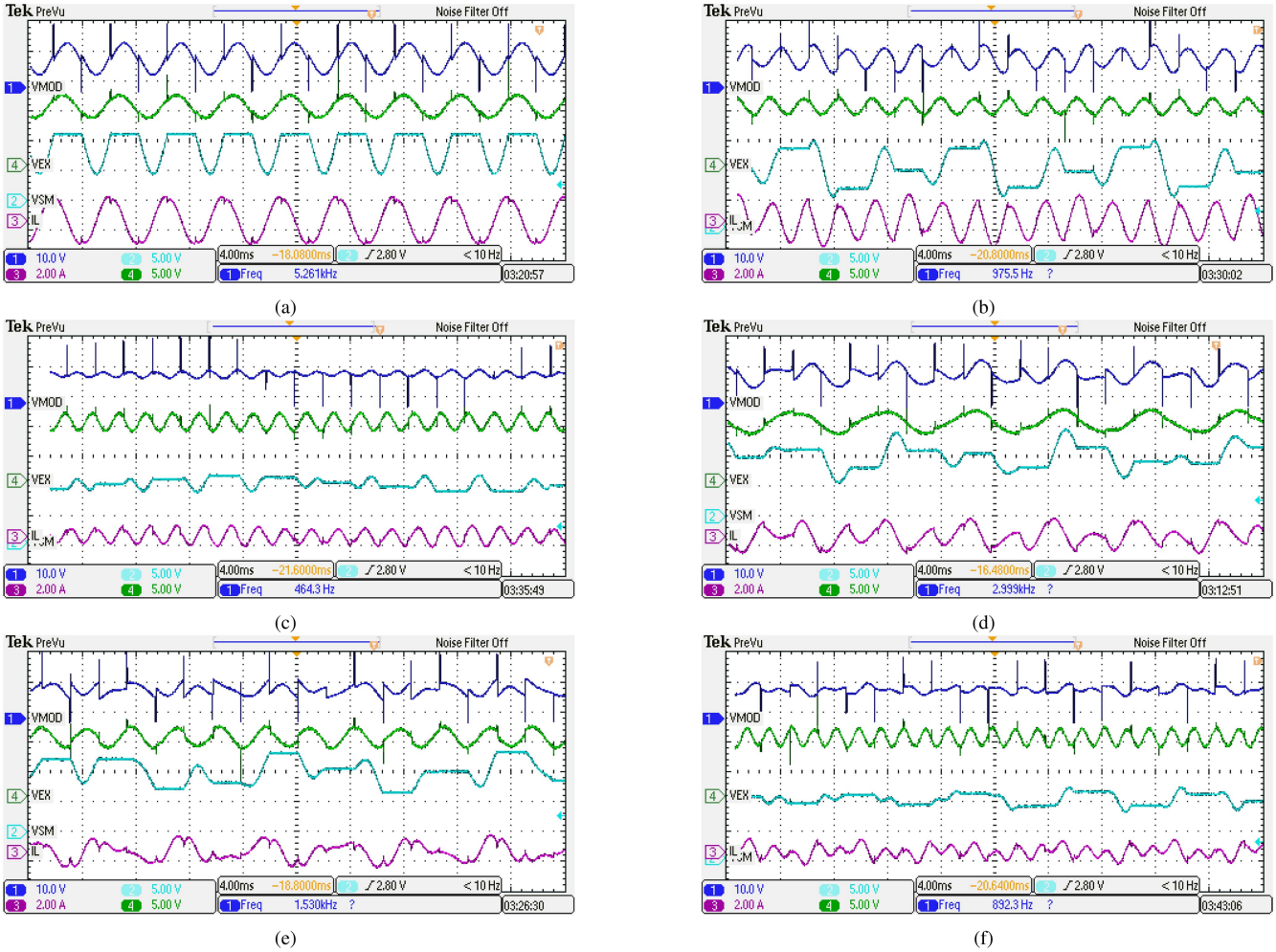

Fig. 21. Experimental results in response to ripple frequencies at the dc link-V_{mod} (first plot from top), dc link voltage with ripple frequency (second plot), SM capacitor voltage (third plot) and arm inductor current (fourth plot) at, (a) Invariant Resonant Frequency (236 Hz), (b) Variant Resonant Frequency (394 Hz), (c) 500 Hz, (d) 150 Hz, (e) 300 Hz, (f) 600 Hz.

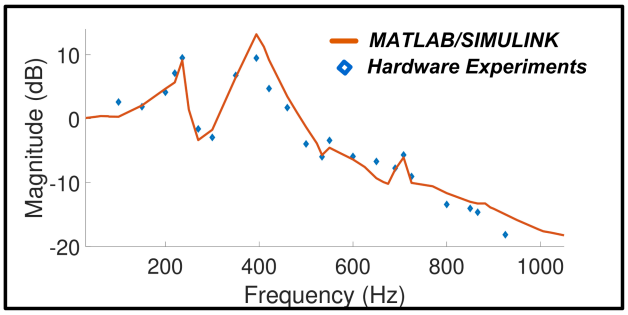

Fig. 22. Experimental results from hardware setup (blue diamonds) overlayed with MATLAB/SIMULINK simulations (orange solid line).

in Fig. 20. The PWM pulses for the MMC submodules are implemented on the Zynq7000/Zedboard FPGA platform. The switching frequency of the HF-MMC was chosen as 236 Hz. This frequency was chosen because the Chroma ac+dc power supply could inject ripples in the dc link till a maximum frequency of 1000 Hz. A total arm inductance of 2.5 mH and submodule capacitance was 80 μF was used in the experiment. The VRF peak falls at 394 Hz for these parameters. The dc link voltage was chosen as 20 V and small voltages of amplitude 2.5 V at various frequencies from 100 Hz − 1000 Hz was injected into the dc link to study the frequency response of the HF-MMC submodules.

In Fig. 21 are shown the submodule capacitor voltage, V_{mod}, arm inductor current and the external voltage applied at the dc link for various frequencies of ripple. The capacitor voltages and inductor currents complete a period in N_{gcd} cycles of switching frequency. The ratio of the amplitude of V_{mod} to the amplitude of applied ripples at various frequencies of ripple are plotted in Fig. 22. The various resonant peaks match the theoretical predictions for these frequencies. This confirms the analysis of the frequency response of the HF-MMC phase legs to dc link ripples as detailed in this study.

VII. Conclusion

The dc side frequency domain characterization of the HF-MMC phase legs was performed and it was shown that the frequency response of the sum of submodule output voltages is

dominated by resonant peaks at frequencies called as the invariant, variant and follower resonant frequencies. Correspondingly, closed-form expressions of the frequencies of these peaks were presented. It was observed that the major resonant peak lies at the link frequency or the switching frequency of the HF-MMC. This resonant peak is largely insensitive to the changes in the inductance and capacitance values forming the series R-L-C network. Through results from MATLAB/SIMULINK,OPAL-RT Hardware-In-Loop, and the hardware experimental setup, the magnitude and phase response plots from the model was observed to match closely with the analytical results.

ACKNOWLEDGMENT

The authors would like to sincerely thank Prof. Bernardo Cockburn, Mathematics Department, University of Minnesota, for the fruitful discussions and for helping out with the formulation of the problem in Section III-C.

REFERENCES

[1] M. R. Islam, Y. Guo, and J. Zhu, "A high-frequency link multilevel cascaded medium-voltage converter for direct grid integration of renewable energy systems," *IEEE Trans. Power Electron.*, vol. 29, no. 8, pp. 4167–4182, Aug. 2014.

[2] M. R. Islam, A. M. Mahfuz-Ur-Rahman, M. M. Islam, Y. G. Guo, and J. G. Zhu, "Modular medium-voltage grid-connected converter with improved switching techniques for solar photovoltaic systems," *IEEE Trans. Ind. Electron.*, vol. 64, no. 11, pp. 8887–8896, Nov. 2017.

[3] B. Zhao, Q. Song, J. Li, and W. Liu, "A modular multilevel DC-link front-to-front DC solid-state transformer based on high-frequency dual active phase shift for HVDC grid integration," *IEEE Trans. Ind. Electron.*, vol. 64, no. 11, pp. 8919–8927, Nov. 2017.

[4] B. Zhao, Q. Song, J. Li, X. Xu, and W. Liu, "Comparative analysis of multilevel-high-frequency-link and multilevel-DC-link DC–DC transformers based on MMC and dual-active bridge for MVDC application," *IEEE Trans. Power Electron.*, vol. 33, no. 3, pp. 2035–2049, Mar. 2018.

[5] J. Shi, W. Gou, H. Yuan, T. Zhao, and A. Q. Huang, "Research on voltage and power balance control for cascaded modular solid-state transformer," *IEEE Trans. Power Electron.*, vol. 26, no. 4, pp. 1154–1166, Apr. 2011.

[6] Q. Zhu, L. Wang, A. Q. Huang, K. Booth, and L. Zhang, "7.2-kV single-stage solid-state transformer based on the current-fed series resonant converter and 15-kV SiC MOSFETs," *IEEE Trans. Power Electron.*, vol. 34, no. 2, pp. 1099–1112, Feb. 2019.

[7] "How a wind turbine works," [Online]. Available: https://www.energy.gov/eere/wind/animation-how-wind-turbine-works

[8] Sie, "Siemens wind turbines." Accessed: Feb. 15, 2025. [Online]. Available: https://pdf.archiexpo.com/pdf/siemens-gamesa/swt-23-108/88089-134481.html

[9] "Siemens HVDC plus," 2017. [Online]. Available: https://www.energy.siemens.com/us/en/power-transmission/hvdc/hvdc-plus/

[10] "US energy information administration," [Online]. Available: https://www.eia.gov/outlooks/aeo/pdf/electricity_generation.pdf

[11] "Forecast international's energy portal." Accessed: Feb. 15, 2025. [Online]. Available: https://ieefa.org/resources/ieefa-us-surging-generation-solar-wind-track-push-renewable-market-share-30-percent-2026

[12] "Renewables are outgrowing their grids," 2016. [Online]. Available: https://www.technologyreview.com/2016/10/13/156998/in-china-and-germany-renewables-are-outgrowing-their-grids/

[13] A. K. Sahoo and N. Mohan, "A power electronic transformer with sinusoidal voltages and currents using modular multilevel converter," in *Proc. Int. Power Electron. Conf.*, May 2014, pp. 3750–3757.

[14] A. K. Sahoo and N. Mohan, "High frequency link multi-winding power electronic transformer using modular multilevel converter for renewable energy integration," in *Proc. 40th Annu. Conf. IEEE Ind. Electron. Soc.*, Oct. 2014, pp. 4642–4648.

[15] A. Sahoo, "Modular converter with multilevel submodules," [Online]. Available: https://patents.google.com/patent/US20150124506

[16] V. N. Vipin, A. Kshirsagar, and N. Mohan, "Utility scale interface for renewables and storage using a power electronic transformer with back-to-back MMCs: A novel proposal and control scheme for virtual inertia," in *Proc. IEEE Energy Convers. Congr. Expo.*, Sep. 2018, pp. 1–5.

[17] V. N. Vipin, A. Kshirsagar, D. Opila, and N. Mohan, "Utility scale interface for renewables and storage using a power electronic transformer with back-to-back MMCs: A novel control scheme," in *Proc. North Amer. Power Symp.*, Sep. 2017, pp. 1–6.

[18] V. N. Vipin, D. Venkatramanan, and N. Mohan, "An online-optimization-based high-frequency link control of an MMC-driven power electronic transformer for wind-energy systems," *IEEE Trans. Energy Convers.*, vol. 38, no. 3, pp. 1986–1998, Sep. 2023.

[19] W. A. Reass, D. M. Baca, and R. F. Gribble, "Components and technologies for high frequency and high average power converters," Apr. 2008. [Online]. Available: https://www.nist.gov/system/files/documents/pml/high_megawatt/Reass.pdf

[20] "Nanocrystalline soft magnetic material finemet," [Online]. Available: http://www.hilltech.com/pdf/hl-fm10-cFinemetIntro.pdf

[21] J. Lyu, X. Zhang, X. Cai, and M. Molinas, "Harmonic state-space based small-signal impedance modeling of a modular multilevel converter with consideration of internal harmonic dynamics," *IEEE Trans. Power Electron.*, vol. 34, no. 3, pp. 2134–2148, Mar. 2019.

[22] J. Lyu, X. Cai, and M. Molinas, "Frequency domain stability analysis of MMC-based HVDC for wind farm integration," *IEEE Trans. Emerg. Sel. Topics Power Electron.*, vol. 4, no. 1, pp. 141–151, Mar. 2016.

[23] R. Vidal-Albalate, H. Beltran, A. Rolán, E. Belenguer, R. Peña, and R. Blasco-Gimenez, "Analysis of the performance of MMC under fault conditions in HVDC-based offshore wind farms," *IEEE Trans. Power Del.*, vol. 31, no. 2, pp. 839–847, Apr. 2016.

[24] V. N. Vipin, D. Venkatramanan, and N. Mohan, "Grid integration of heterogeneous energy sources/loads using a multi-port MMC with independent power flow," in *Proc. IECON 47th Annu. Conf. IEEE Ind. Electron. Soc.*, 2021, pp. 1–6.

[25] M. Vasiladiotis, S. Kenzelmann, N. Cherix, and A. Rufer, "Power and DC link voltage control considerations for indirect AC/AC modular multilevel converters," in *Proc. 14th Eur. Conf. Power Electron. Appl.*, Aug. 2011, pp. 1–10.

[26] R. Picas, J. Pou, S. Ceballos, J. Zaragoza, G. Konstantinou, and V. G. Agelidis, "Optimal injection of harmonics in circulating currents of modular multilevel converters for capacitor voltage ripple minimization," in *Proc. IEEE ECCE Asia Downunder*, Jun. 2013, pp. 318–324.

[27] X. He, J. Peng, P. Han, Z. Liu, S. Gao, and P. Wang, "A novel advanced traction power supply system based on modular multilevel converter," *IEEE Access*, vol. 7, pp. 165018–165028, 2019.

[28] K. Sekiguchi, P. Khamphakdi, M. Hagiwara, and H. Akagi, "A grid-level high-power BTB (back-to-back) system using modular multilevel cascade converters withoutcommon DC-link capacitor," *IEEE Trans. Ind. Appl.*, vol. 50, no. 4, pp. 2648–2659, Jul./Aug. 2014.

[29] M. Li et al., "Four-port modular multilevel AC/AC converter in continuous co-phase traction power supply application," in *Proc. IEEE Energy Convers. Congr. Expo.*, 2020, pp. 1477–1481.

[30] L. Bessegato, L. Harnefors, K. Ilves, and S. Norrga, "A method for the calculation of the AC-side admittance of a modular multilevel converter," *IEEE Trans. Power Electron.*, vol. 34, no. 5, pp. 4161–4172, May 2019.

[31] L. Bessegato, K. Ilves, L. Harnefors, and S. Norrga, "Effects of control on the AC-side admittance of a modular multilevel converter," *IEEE Trans. Power Electron.*, vol. 34, no. 8, pp. 7206–7220, Aug. 2019.

[32] J. Sun and H. Liu, "Sequence impedance modeling of modular multilevel converters," *IEEE Trans. Emerg. Sel. Topics Power Electron.*, vol. 5, no. 4, pp. 1427–1443, Dec. 2017.

[33] I. A. Gowaid, G. P. Adam, A. M. Massoud, S. Ahmed, D. Holliday, and B. W. Williams, "Quasi two-level operation of modular multilevel converter for use in a high-power DC transformer with DC fault isolation capability," *IEEE Trans. Power Electron.*, vol. 30, no. 1, pp. 108–123, Jan. 2015.

[34] I. A. Gowaid, G. P. Adam, S. Ahmed, D. Holliday, and B. W. Williams, "Analysis and design of a modular multilevel converter with trapezoidal modulation for medium and high voltage DC-DC transformers," *IEEE Trans. Power Electron.*, vol. 30, no. 10, pp. 5439–5457, Oct. 2015.

[35] A. Ahmad, M. S. Alam, and R. Chabaan, "A comprehensive review of wireless charging technologies for electric vehicles," *IEEE Trans. Transp. Electrific.*, vol. 4, no. 1, pp. 38–63, Mar. 2018.

[36] J. Choi, J. Xu, R. Makhoul, and J. M. R. Davila, "Implementing an impedance compression network to compensate for misalignments in a wireless power transfer system," *IEEE Trans. Power Electron.*, vol. 34, no. 5, pp. 4173–4184, May 2019.
[37] Z. Ke et al., "Capacitor voltage ripple estimation and optimal sizing of modular multi-level converters for variable-speed drives," *IEEE Trans. Power Electron.*, vol. 35, no. 11, pp. 12544–12554, Nov. 2020.
[38] J. Min and M. Ordonez, "Bidirectional resonant CLLC charger for wide battery voltage range: Asymmetric parameters methodology," *IEEE Trans. Power Electron.*, vol. 36, no. 6, pp. 6662–6673, Jun. 2021.
[39] D. Ewins, *Modal Testing: Theory and Pract.*, ser. Engineering dynamics series. Hoboken, NJ, USA: Wiley, 1984. [Online]. Available: https://books.google.com/books?id=5lYwngEACAAJ

Vishnu Narayan Vipin (Member, IEEE) received the B.Tech. degree in electrical and electronics engineering from the National Institute of Technology (NIT), Trichy, India, in 2015, and the M.S. and Ph.D. degrees in electrical and computer engineering from the University of Minnesota, Minneapolis, MN, USA, in 2021.

From 2021 to 2022, he worked with in the R&D team, SolarEdge Technologies, Milpitas, CA, USA, and currently works with Rivian Automotive, Torrance, CA, USA, in the power electronics controls group. His current research interests include topologies and control for grid integration of renewables, chargers for electric vehicles, and controls design of power converters.

Ned Mohan (Fellow, IEEE) (October 5, 1946–February 11, 2024) received the bachelor's degree in electrical engineering from the Indian Institute of Technology Kharagpur, West Bengal, India, in 1967, and the master's degree in nuclear engineering and the Ph.D. degree in electrical engineering from the University of Wisconsin–Madison, WI, USA, in 1972 and 1973, respectively.

He was the Oscar A. Schott Professor of power electronics with the University of Minnesota, Minneapolis, MN, USA, where he had been engaged in teaching since 1976. He was elevated to Fellow of the IEEE in 1996, inducted into the U.S. National Academy of Engineering in 2014, and instituted as a Regents Professor with the University of Minnesota in 2019. He has numerous patents and publications in the fields of power electronics, electric drives, and power systems. He has authored or coauthored five textbooks, one of which has been translated into six languages.

Dr. Mohan was the recipient of several accolades from the IEEE and pertinent societies, including the 2008 IEEE PES Outstanding Educator Award, 2010 IEEE Undergraduate Teaching Award, 2010 UWIG Achievement Award from Utility Wind Integration Group, 2011 Distinguished Alumnus Award from IIT Kharagpur, 2012 IEEE Power and Energy Society Ramakumar Family Renewable Energy Excellence Award, the Innovative Program Award from the ECE Department Heads Association made up of over 250 universities in the United States in 2013, the IEEE PES Nari Hingorani FACTS Award in 2014, the IEEE Industrial Applications Society Educator/Mentor inaugural award in 2019, and the 2022 IEEE James H. Mulligan, Jr. Education Medal. He set up CUSP: Consortium of Universities for Sustainable Power, which curated various educational materials at graduate and undergraduate levels.